

Color centers in wide-bandgap semiconductors for subdiffraction imaging: a review

Stefania Castelletto^{a,*} and Alberto Boretti^b

^aRMIT University, School of Engineering, Bundoora, Australia

^bPrince Mohammad Bin Fahd University, Deanship of Research, Al Khobar, Saudi Arabia

Abstract. Solid-state atomic-sized color centers in wide-band-gap semiconductors, such as diamond, silicon carbide, and hexagonal boron nitride, are important platforms for quantum technologies, specifically for single-photon sources and quantum sensing. One of the emerging applications of these quantum emitters is subdiffraction imaging. This capability is provided by the specific photophysical properties of color centers, such as high dipole moments, photostability, and a variety of spectral ranges of the emitters with associated optical and microwave control of their quantum states. We review applications of color centers in traditional super-resolution microscopy and quantum imaging methods, and compare relative performance. The current state and perspectives of their applications in biomedical, chemistry, and material science imaging are outlined.

Keywords: color centers; quantum optics; single photon emitters; super-resolution imaging; transparent semiconductors.

Received May 21, 2021; revised manuscript received Jul. 13, 2021; accepted for publication Aug. 19, 2021; published online Sep. 13, 2021.

© The Authors. Published by SPIE and CLP under a Creative Commons Attribution 4.0 International License. Distribution or reproduction of this work in whole or in part requires full attribution of the original publication, including its DOI.

[DOI: [10.1117/1.AP.3.5.054001](https://doi.org/10.1117/1.AP.3.5.054001)]

1 Introduction

The resolution of common fluorescence microscopes (wide-field or confocal microscopes) is limited by the diffraction of light, known as the Abbe limit. The attainable resolution is given by the full-width at half-maximum (FWHM) of the point spread function (PSF) of the beam at the focus of the objective. A high numerical aperture (NA = 1.4) objective with visible light ($\lambda = 532$ nm) can theoretically reach a resolution of $d \approx \lambda / (2\sqrt{2} \times \text{NA}) \sim 134$ nm and $d \approx \lambda / (2 \times \text{NA}) \sim 190$ nm for the confocal and wide field, respectively, whereas the experimental resolution is generally in the range of ~ 200 to 250 nm due to the sample optical properties and beam imperfections. Super-resolution fluorescence microscopy (SRM) permits us to beat the diffraction limit, and it obtains images with a higher resolution, from 100 nm to as low as 20 nm or, in some cases, even lower, with few nanometer localization in some cases. This is a resolution/localization possible only by electron scanning probe microscopes. SRM's impact in life science, chemical,

and physical sciences has been recognized by the Nobel Prize for Chemistry in 2014,¹ and it has revolutionized many areas of cellular microscopy² and even virology.^{3,4}

Current SRM methods have resolved many problems in imaging using high localization molecules, with the opportunity to reach a very high resolution in principle. In general, they can provide high spatial localization and resolution with, however, limited applicability in tracking real-time biological processes with the required speed. In addition, the application of the currently achieved ultimate resolution in some of the SRM methods to specific biological samples, with associated high localization and the required sensitivity, is a prerequisite that is not yet fully achieved.

The current outstanding limitations in a few SRM approaches are

- the size of the fluorescent probes and their fluorescent properties;
- the use of near-ultraviolet excitation which is responsible for DNA damage and higher imaging background, reducing applicability for extended imaging time and tracking;
- the photobleaching of the fluorescent tags, which limits the duration of observation;

*Address all correspondence to Stefania Castelletto, stefania.castelletto@mit.edu.au

- the extended acquisition or scanning time needed to achieve the highest resolution, which limits the imaging speed and applicability for *in vivo* imaging and tracking;
- lack of achievement of in-depth imaging with the same high in-plane resolution.

Among these limitations, the type and size of the fluorescent tags are extremely important to directly access the subdiffraction biological components and features of interest, achieve the desired resolution in the cells' environment, follow internal biological mechanisms in cells, and track cellular processes at specific locations. The quest for ideal SRM tags is to have probes that introduce as few as possible artifacts in imaging and have limited interaction with the sample functionalities. They must possess photophysical properties fulfilling the requirements of the SRM principles. They should not photobleach. Furthermore, depending on the process that needs to be imaged, the fluorophores with distinct fluorescence properties are sought after first and foremost, for their brightness, fluorescence lifetime, photostability, emission wavelength, and, as in some cases, photoswitching capabilities. While these properties are essential for advancing the application of SRM to biological samples, they are also important for applications in imaging in material science, chemistry, and physics. Other emerging applications of SRM, where in particular color centers (CCs) in diamond have also been utilized, are optical data storage,^{5,6} imaging of current flow at the nanoscale as an example in two-dimensional (2D) materials, such as graphene,⁷ and using quantum magnetometry to study magnetic optical effects in solid state.⁸ Many fluorescent nanoprobe are now available for SRM, and, more recently, solid-state probes based on nanoparticles (NPs) have been investigated for these applications⁹ in virtue of their high brightness, high photostability, and unique optical-switching properties in addition to other physical and chemical functionalities. CCs in wide-bandgap semiconductors, in particular, have emerged as potential atomic size probes (which is an ultimate quest), due to their extreme photostability, lack of bleaching also in the presence of high laser power density, high dipole moment, generally long optical transition lifetime, and available long life metastable (MS) state. In addition, CCs can exist in various charge states, and photoswitching between them can be achieved using different laser excitation wavelengths. Finally, most of the CCs have a nonzero electron spin, which can be read out optically and can serve as a probe of the local magnetic and electric field, as well as of local strain. Fluorescence modulation of CCs can be achieved by nonspin preserving transitions into the MS state, inducing spin polarization of a degenerate ground state (GS). The manipulation of the spin properties using the additional microwave or radiofrequency excitations can also provide an extra-nonlinear optical response to be used in super-resolution approaches. The most notable material hosting CCs is diamond, with a large variety of emitters mostly studied in bulk diamond,^{10,11} and, specifically, the most studied is the nitrogen-vacancy (NV) center.¹² Diamonds and nanodiamonds (NDs) are currently widely studied nanoprobe due to their biocompatibility and low phototoxicity in various medicine applications.¹³ Diamond has been recently followed by silicon carbide (SiC)^{14,15} with the carbon antisite vacancy pair (CAV),^{16,17} divacancy (DV),^{18,19} and interface defects.²⁰ SiC and its nanostructures have also been studied as biological nanosensors, nanocarriers, and biomedical applications.^{21–23} Other wide-bandgap materials, such as 2D

hexagonal boron nitride (hBN), which have driven the attention in photonics and single-photon (SP) emission,^{24,25} have also shown applicability to conventional super-resolution methods²⁶ due to a variety of functionalization options and low cells toxicity,^{27,28} albeit only a few studies are available today. We will briefly assess the current state of the art of these three materials' CCs for their performance in SRM. While the diamond NV center has been the first to be used for SRM for more than 10 years,²⁹ proving to be a robust system to push the limit of the present SRM methods accuracy, its applicability as fluorescent probes even in traditional SRM methods is still limited. This is due to the current limitation of CCs embedded in NPs, with relatively large size, which has currently limited application in traditional SRM.⁹ However, some of the best resolutions achieved, biocompatibility and photostability for biological *in vitro* and living samples imaging, are associated as an example to NDs.³⁰ The only limitation is the lack of availability of highly performing CCs photophysical and spin properties in single-digit size NDs as their quantum dots (QDs) counterparts. Using NV centers as probes, the first traditional SRM methods have been demonstrated, such as stimulated emission depletion (STED) microscopy,²⁹ ground-state depletion (GSD) microscopy,³¹ MS state depletion³² microscopy, and stochastic optical reconstruction microscopy (STORM).³³ From the initial SRM demonstrated using NV in diamond, other variants of these methods were proposed and implemented,³⁴ and we can, after 10 years, observe a certain degree of advances in using specific photophysical properties of this CC in SRM. In addition, using the NV center in diamond, nontraditional SRM methods have been developed to achieve subdiffraction images based on their specific photophysical properties. Defect charge conversion upon different illumination energy [charge state depletion (CSD) microscopy³⁵] and spin fluorescence modulation based on optical detected magnetic resonance (ODMR)¹² are examples of properties used to achieve super-resolved images of NV in diamond. This last approach based on the electron spin readout of NV, used as a sensor of other nearby electron and nuclear spins, in particular, is leading toward nano magnetic resonance imaging (MRI)³⁶ or nuclear magnetic resonance (NMR) spectroscopy,³⁷ showing at present few nuclear spins or single electron spin sensitivity (nano MRI or NMR). These methods are borrowed from MRI approaches and adjusted to operate using an atomic-scale quantum probe rather than a magnetic field coil. They are based on the implementation of electron spin-echo, Hanh-echo sequence,^{38,39} or more complex dynamical spin decoupling sequences.^{40,41} Here, the readout is based on the optical signal of NV centers. Recent focus on the use of NV in diamond as a magnetic sensor⁴² designed for biological living systems has reached, even in DC magnetometry, the sensitivity of 100 pT/ $\sqrt{\text{Hz}}$,⁴³ and, by using a lock-in-based technique to read out optically the NV spin, a sensitivity of 68 nT/ $\sqrt{\text{Hz}}$ within the (sub)cellular scale has been achieved.⁴⁴ As such, the quantum properties of CCs can be used or combined with traditional SRM that does not rely on the quantum nature of the nanoprobe but on their nonlinear optical properties or on their nonstationary fluorescence, which makes them discernible from one to another. The combination of quantum magnetic imaging methods with super-resolution localization can lead to nanoscale magnetic sensing and imaging with subdiffraction localization. In this direction, using NV centers in diamond, a variant of traditional SRM, has been implemented using ODMR to address single or ensemble spin with super-resolved localization; namely

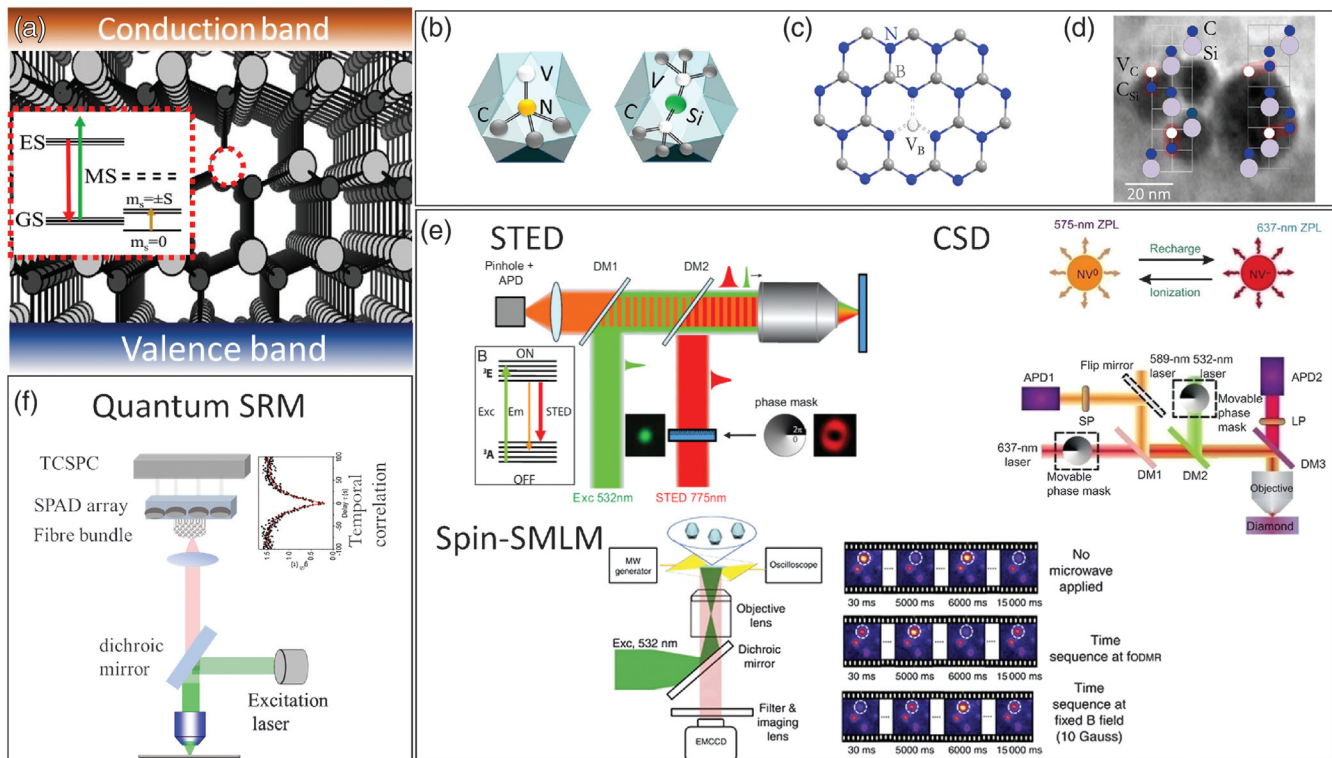


Fig. 1 CCs and traditional and quantum SRM. (a) Conceptual representation of a vacancy in a wide bandgap semiconductor, giving origin to a three or more levels system made of a ground state (GS) (with spin triplets, depending on the spin number), an excited state (ES), and a meta-stable state (MS) or intersystem crossing state. (b) The NV and the SiV in diamond are used for SRM methods. (c) 2D hBN showing the boron vacancy. (d) The CAV pairs that can be used for SRM due to their photoswitching properties.⁵⁹ (e) Traditional SRM methods schematics such as STED, based on depletion of ES via stimulated emission, and SMLM as fully nondeterministic methods, based on the photoswitching of the fluorophore. CSD microscopy originated from the charge conversion of NV from the negative to neutral state, using three laser probes in a more complex approach than STED. STED figure is reproduced from Ref. 60; with permission copyright (2010) John Wiley and Sons, Inc., CSD and Spin-SMLM figures are reproduced from Refs. 48 and 35, under Creative Commons Attribution-NonCommercial-NoDerivs (BY-NC-ND) 4.0 International license. A detailed description of the schematics is provided in the references. (f) Conceptual schematics of the quantum-enhanced SRM developed based on antibunching, giving rise to the mapping of localized single emitters from the spatial imaging of single emitters using a bundle of fibers and array of SPADs and time-correlated single-photon counting (TCSPC).⁵⁷

STED-ODMR,⁴⁵ SPIN-RESOLFT,⁴⁶ and SPIN-STORM^{47–49} have been extended to achieve spin localization using ODMR and other spin manipulation methods used in AC magnetometry, primarily spin-echo sequences.⁵⁰ Even some dynamical spin decoupling sequences are used in the nano-MRI to increase the sensitivity of dilute ensembles of nuclear spins or single electron spin. These methods have been developed in the NV quantum sensing approaches and led to relevant imaging capability, for example, sensing ferritin in single cells,⁵¹ single electron spin,⁵² and electron flow in graphene.⁵³ The combination of increased sensitivity from quantum sensing with nanometric localization and tracking is a very sought-after objective that could be achieved using the quantum properties of CCs. Alternatively, using the quantum optical properties of single CCs as SP sources, quantum imaging methods based on SP higher-order correlation have been developed to achieve subdiffraction imaging.^{54,55} These quantum methods can also be used to enhance conventional

SRM, such as quantum-enhanced STORM.^{56,57} One of the most promising applications of NV centers in NDs is to achieve highly localized temperature sensing,⁵⁸ which could be combined with super-resolution methods. In addition to the most notable NV in diamond, other CCs in diamond, mainly silicon-vacancy (SiV), in SiC, and few layers of hBN have emerged as possible tools for SRM; alternatively, these CCs can be better studied using SRM. In Fig. 1, illustrations of examples of CCs used for traditional and quantum-based SRM with their conceptual operation are shown. In Table 1, we summarize the CCs properties in diamond, SiC, and hBN that have been tested or recognized as relevant for SRM applications, such as emission wavelength, quantum yield or quantum efficiency, excited state (ES) and MS or intersystem state lifetimes, known coexisting charge states, stimulated emission cross-section, optical spin coherence time, SP availability, and nanomaterial associated properties when available. Compared with other solid-state

Table 1 CCs in diamond, SiC, and hBN flakes with charge states, ZPL, and their optical and spin properties relevant for SRM and quantum enhanced SRM. Specifically, the negative charge state of NV and SiV in diamond, the NVN (H3) center in diamond, the positive CAV pair, the neutral DV in SiC, the negative boron vacancy V_B^- and the complex boron vacancy and carbon–nitrogen antisite $V_B C_N^-$. Properties such as quantum yield (η), fluorescence lifetime (τ_{fl}), intersystem crossing lifetime (τ_{ISC}), stimulated emission cross section (σ), and spin coherence time (T_2) are listed. NDs sized 25 to 100 g nm, SiC NPs of 3 to 50 nm. All of the below CCs have been isolated as single emitters except the V_B^- . Here, n.m. stands for not measured and n.a. for not available.

Color center	ZPL (nm)	η (%)	τ_{fl} (ns)	τ_{ISC} (ns)	$\sigma \times 10^{-17}$ (cm ²)	T_2 (μ s)
NV ^{-/0} C-bulk	637	70 ²⁹	11.7	150 × 10 ⁹ ⁶¹	1.2 ²⁹	2400 ⁶²
NV ^{-/0} NDs	637	23 to 90	21.4 to 22.8	300 ^{63–68}	—	0.44 to 1.27 ⁶⁹
SiV ^{-/0} C-bulk	738	0.5 ⁷⁰	1.78	22.4 ⁷¹	4 ⁷²	0.035 (T_2^*) ⁷³
SiV ^{-/0} NDs	738	0.3 to 9.2 ⁷⁴	0.23 to 1.3 ⁷⁵	1200 to 9100 ⁷⁴	—	n.m.
NVH NDs	503	95	27, ⁷⁶ 40 ⁷⁷	—	2.1	n.m.
CAV ^{+/0} ¹⁶ 4H-SiC-bulk	648	70	1.8	40	—	n.a.
CAV ^{+/0} 3C-SiC-NPs ¹⁷	645	—	2.1 to 5.3	300 to 800	—	n.a.
DV ^{0/+} 4H-SiC-bulk	1100	—	14	—	—	1200 ^{18,19}
DV ^{0/+} 4H-SiC-NPs ⁷⁸	1100	—	—	—	—	n.m.
N _C V _{Si} ⁻ 4H-SiC-bulk ⁷⁹	1230	98	2.4 to 2.8	601 to 684	—	17.2 ^{80,81}
V _B C _N ⁻ hBN ^{82,83}	571	65 to 95 ⁸⁴	3.58	167 to 833 ⁸⁴	5.5 to 10 ⁸⁵	n.m.
V _B ⁻ hBN ⁸⁶	850	—	1.2	—	—	2 ⁸⁷

emitters, most of the diamond CCs are in the red spectral region (except for the H3 center) and do not need to use UV excitation. For SiC, there are emitters in red as in diamond and emission toward infrared (IR), providing also reduced scattering of the excitation laser (780 or 980 nm) for depth imaging. hBN emitters are from green to red and require excitation mostly at 532 nm or below; however, two-photon excitation with a 780-nm laser can be achieved in some emitters. Details of CCs in these materials can be found in a specific recent review,^{11,15,26} whereas, here, the summary is done only of the centers used in SRM. Details of which properties are relevant for the specific SRM methods are discussed in the related sections of this paper. In this paper, we review the current diamond, SiC, and hBN CCs status of their applications in SRM, and we look at their possible applicability in SRM and quantum sensing as well as in quantum super-resolution methods. We first review traditional SRM methods applied to CCs in diamond, SiC, and hBN and compare their relative properties. We consider the variant of traditional SRM methods applied to these emitters together with the spin sensing capabilities to determine state of the art spin nanoscopy and their applications. Then, we review the so-called quantum-enhanced SRM methods developed using the quantum optics properties, such as SP emission or sub-Poissonian statistics. We show their performances in comparison with conventional methods and current use of CCs in this space.

2 Traditional Super-Resolution Microscopy Methods and Their CCs Variant

SRM principles rely upon switching off the fluorescence of the samples in a subdiffraction limited area using the modulation of the photophysical properties of the fluorophores and spatial control of the excitation beam. Two major groups of far-field SRM methods are generally identified depending on the fluorescence tags' physical processes used and on the image reconstruction

methods, based on the switching mechanism either deterministic or stochastic. SRM deterministic methods rely on the non-linear optical response of the fluorophore to the excitation laser, e.g., by exciting the fluorophore from its GS to the ES and then delving into its dark state with two or more excitation beams as in STED,⁸⁸ GSD,⁸⁹ MS state depletion⁹⁰ microscopy, and reversible saturable optical fluorescence transitions (RESOLFT) microscopy.⁹¹ In STED and GSD microscopies, the dark state is a GS, whereas, in the other methods, the dark state is a long-lived MS state or intersystem crossing state. Among deterministic methods, structural illumination microscopy (SIM) is based on excitation using the spatially structured pattern of light-generating interference patterns, whose mathematical deconvolution provides super-resolution images with a lateral resolution in 100 nm.⁹² Stochastic methods rely on the chemical (such as oxidation or redox or electron tunneling) complex properties of many single nanoemitters showing photoswitching behavior at separate times, so nanometric distant fluorophores can be resolvable in time and then localized. The time localization is then converted into spatial localization using specific algorithms deconvolving each fluorophore point spread function (PSF). These methods are known as single-molecule switching or localization microscopy (SMLM) divided into photoactivation localization microscopy (PALM)⁹³ and STORM.⁹⁴ An additional variation of these methods depends on the used fluorophores and their photochemistry properties, and they can achieve super-resolution in 2D or 3D. As a common feature, these methods permit us to achieve spatial resolution below 100 nm, enabling the imaging of nanometric entities for the examination of their architectural details and their interactions with other systems, mostly biological samples and cell constituents. These methods permit the resolution of images better than 20 nm and achieve 10-nm localization accuracy. While high resolution can be achieved with these methods, they suffer from slow acquisition time and/or postprocessing of images, as well as in some cases of phototoxicity or photobleaching of

fluorescent tags that make volumetric time elapse imaging of living samples impractical. Recent reviews presenting the working principles of these methods and the main complementary achievements and advantages can be found in Refs. 2, 95, and 96. Here, briefly, we repeat that deterministic methods generally require higher optical power than nondeterministic methods, having the first as a major advantage in real-time imaging that is not possible with nondeterministic methods requiring postprocessing and longer acquisition time. As such, nondeterministic methods such as SMLM are less suitable for *in vivo* imaging regardless of their better resolution.

3 Stimulated Emission Depletion Microscopy

The STED microscopy conceptual framework was first proposed more than 25 years ago.⁸⁸ Details of how to build a STED microscope today are reviewed in Ref. 97. In STED, a fluorescent probe is first excited by light from the GS to an ES, and then it is either de-excited by applying a STED beam via stimulated emission or, spontaneously, via fluorescence emission. To efficiently force a fluorophore to the GS, the stimulated emission rate has to be faster than the spontaneous emission rate, i.e., the inverse of the optical lifetime, τ_{fl} , which typically occurs within a few nanoseconds after the excitation event. The fluorescent subdiffraction spots in STED are obtained by scanning the sample with a coaligned Gaussian excitation beam with a second excitation beam tuned in wavelength to achieve stimulated emission and engineered with a doughnut-shaped focal intensity distribution corresponding to a “zero”-intensity point in the center. This second beam is also known as the STED beam, and it is tuned generally in the phonon side band of the emitter.

The expected resolution is given as

$$d \approx \frac{\lambda_{\text{STED}}}{2 \times \text{NA} \times (1 + aI_{\text{max}}/I_s)} \sim 50 \text{ nm}, \quad (1)$$

where I_{max} is the maximum STED beam intensity, I_s is the stimulated emission saturation intensity of the fluorophore, and a takes into account a nonperfect doughnut-shaped STED beam. The stimulated emission rate is given by $\sigma \times I_{\text{STED}} \times \lambda_{\text{STED}}/(hc) \gg 1/\tau_{\text{fl}}$, where σ is the stimulated emission cross section. The advantage of STED microscopy is the real-time creation of the super-resolved image with a simple acquisition process, without the need of image postprocessing, which may induce potential postprocessing image artifacts. However, achieving high resolution and high speed comes at the expense of phototoxicity. When exposing samples with high laser intensities in the level of $\approx \text{GW cm}^{-2}$, as with the STED beam, radicals or singlet oxygen can be generated causing photobleaching and phototoxicity in living systems with subsequent cell death. However, living cell imaging with STED has been achieved^{98,99} by optimizing the sample preparation protocols and using fast beam-scanning methods. Nevertheless, STED microscopy, even if it can be used for fast live cells and fixed cells studies, due to the inevitable still too high laser power required, is less suitable for a long period of live-cell imaging, while its application in imaging the molecular environment in biological systems is widespread.¹⁰⁰

STED was first applied to NV in optical grade bulk diamonds exciting the spontaneous fluorescence emission occurring

between 650 and 750 nm with a 532-nm laser and inducing the stimulated emission of the ES to the GS with a 775-nm laser. The unique properties of NV in diamond for STED are

- the stimulated emission decay rate is much larger than the spontaneous decay rate;
- NV long spontaneous emission lifetime ($\tau_{\text{fl}} = 11.7$ ns in bulk and 23 ns in NDs⁶³);
- high stimulated emission cross-section σ ;
- phononic coupling of its GS enables quenching of the excited NV centers more efficiently;
- NV quantum efficiency is high (0.7);
- NV possesses extreme photostability once probed with a STED beam of $I_{\text{max}} = 3.7 \text{ GW/cm}^2$;
- NV broad emission allows using a quite wide spectral separation of the excitation and STED beams.

Using the STED beam with a Gaussian excitation beam, the spontaneous emission occurred only in the region where the STED beam intensity is zero, that is in the excitation beam center, identifying a subdiffraction emission area, with a resolution between 16 and 80 nm. The record emitter localization was determined to be 8 nm in bulk diamond.²⁹ Later, STED was extended to NDs to permit the application of these nanoprobes to biological samples imaging. NDs as small as 25 nm have been employed where each particle contained up to seven NV centers. 3D super-resolution has been achieved with 50-nm resolution.³² This result has prompted STED applications of fluorescent nanodiamonds (FNDs) and NDs with a high concentration of NV centers, covalently conjugated with bovine serum albumin or α -lactalbumin as markers in cells [Figs. 2(a)–2(c)], achieving a resolution of ≈ 50 nm.¹⁰¹ Other green fluorescent CCs in NDs due to high concentration of N-V-N (or H3) defects were used for STED imaging with 70-nm resolution in the cell environment. Here, green FNDs were used as STED biomarkers up-taken into HeLa cells⁷⁶ [Fig. 2(d)]. In conjunction with NV in FNDs, these CCs provide a way to perform two-color STED observations and to achieve STED correlation imaging, which is used for dynamic nanoscale interactions for *in-vivo* cell studies.¹⁰³ FNDs can also be used as dual-contrast for correlative imaging of high-resolution STED/confocal and transmission electron microscopy (TEM) experiments¹⁰² [Figs. 2(e)–2(g)]. More studies of correlative electron and fluorescence microscopy (CELM) of FNDs have shown that FNDs can withstand electron beam exposure with their fluorescent properties remaining intact for light microscopy.¹⁰⁴ CELM has been used for subdiffraction imaging of antigens CD44 on the HeLa cell surface by FNDs encapsulated in biotinylated lipids with localization of 50 nm.¹⁰⁵ STED has been recently applied to H3 centers in bulk diamond¹⁰⁶ using 470-nm excitation and achieving a resolution of 50 nm. Using these centers in diamond, a departure of the STED resolution from the inverse square-root dependence of the stimulated emission excitation beam intensity is shown, suggesting the presence of charge traps between the ES of the centers and the conduction band.

STED has been applied to the SiV CC in diamond, which exhibits a ZPL at 738 nm; this center possesses better charge stability of the NV, with a two to four times higher stimulated emission cross-section compared to NV,⁷² as shown in Table 1. The STED beam was tuned between 765 and 800 nm. However, the resolution obtained was only 89 nm, limited by the specifically used STED beam pulse energy, whereas it is expected to reach 20 nm with higher energy. As the SiV has been recently

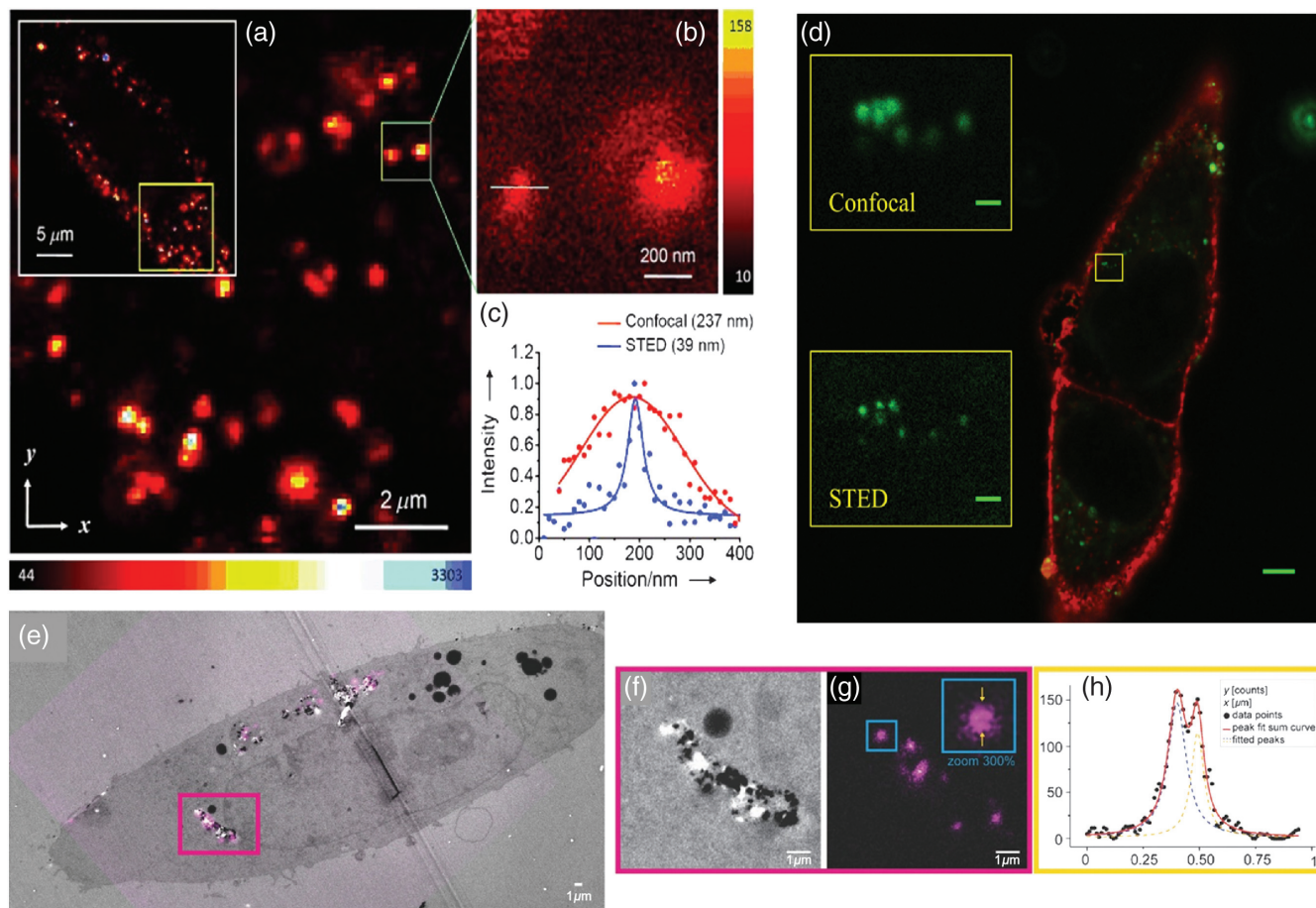


Fig. 2 STED applied to FNDs and green FNDs in cells. (a) Scanning confocal image of a BSA-conjugated NV-FND-labeled cell in the white rectangle. (b) STED image of single BSA-conjugated FND enclosed within the green rectangle in (a). (c) Confocal and STED fluorescence intensity profiles of the FND indicated in (b). Solid curves represent the best fits for Gaussian (confocal) or Lorentzian (STED) functions with the FWHM. Images reproduced with permission from Ref. 101, © 2011 John Wiley and Sons, Inc. (d) Superresolution imaging of green FNDs up-taken into an HeLa cell, which is tagged in red with an organic dye. The main image is a confocal scan. The green FNDs appear green, and the absence of fluorescence inside the cells reveals the positions of the nuclei. The two insets are magnified images of the highlighted area of the cell. Scale bars are 5 μm in the main image and 500 nm in the insets. Images reproduced from Ref. 76, © 2015 Optical Society of America (OSA). STED-TEM correlative imaging of intracellular FNDs in TEM sections. (e) A correlation result on a single cell with TEM in gray and fluorescence signal from FNDs in magenta. (f), (g) Zoomed sections of the correlation result for TEM and STED, respectively. (h) The line profile values of an FND in (g), and a two-peak Lorentzian fit of the data with peaks ≈90 nm apart. Images reproduced with permission from Ref. 102, © 2018 John Wiley and Sons, Inc.

incorporated in 10 nm NDs,¹⁰⁷ this could provide a multicolor STED microscope in a single nanoprobe and compete in the use of CCs-based NDs for STED in biomedical applications. However, the SiV properties in 10-nm NDs have not been studied in detail, even if high brightness was achieved from a single emitter.

STED based on FNDs with red, green, and near-infrared (NIR) emitters has shown very limited applications in biological samples so far due to the large size of NDs, which cannot allow imaging and localization of the 10 nm labeled cell's anatomy features. While the use of STED with NDs has been mostly

driven by a feasibility assessment of achieving higher resolution compared with other currently used fluorophores, the applicability is limited by their size.¹⁰⁸

The spin variant of STED based on NV quantum sensing as described in the next section may have more possibilities to advance their applications in biological science.

Similarly, STED in bulk diamond CCs has not been applied so far in biological samples imaging, while it is sometimes used for the study of the nanoscale photophysical properties of the quantum emitters or to assess their nanoscale fabrication.⁶⁰ For example, the stimulated emission of NV in diamond has

been used to induce lasing in NV, laying the foundation for laser magnetometry.¹⁰⁹ A laser magnetometer could achieve a very high contrast for the NV ODMR and prompt more practical applications of MRI using bulk diamond. STED has been applied to the study of a group of quantum emitters in 2D hBN, which presents a large variety of SP emission^{110,111} from the UV to the NIR. These emitters have been recently identified as carbon related,²⁴ specifically a carbon–nitrogen substitution with boron vacancies. Here, STED was applied to the emitters at 2 to 2.2 eV as a spectroscopic tool for the examination of vibronic states, confirming the assigned origin.⁸² In similar quantum emitters at 580 nm, a variant of STED known as time-gated CW-STED achieved a resolution of 50 nm limited by an objective with NA = 0.8.⁸⁵ The stimulated emission cross-section in these quantum emitters in hBN appears larger than in diamond CCs, showing some promises for biological samples imaging.

3.1 Spin Stimulated Emission Depletion Microscopy

By modifying a STED microscopy system, NV spin states could be imaged and localized with 6 nm accuracy,⁴⁵ later improved to 2.4 nm using a solid immersion lens fabricated directly in the bulk diamond.¹¹² These microlenses are used to locally reduce the depletion beam power. These results established a STED variant method for diamond NV spin nanoscopy. A STED beam was added to a typical pulsed confocal-ODMR setup,¹²

constituted of a 532-nm polarization beam and a microwave pulse tuned to the NV⁻ GS spin transitions with an applied static magnetic field. By adding the STED beam, it was possible to distinguish and control the NV⁻ ODMR signal of five NV⁻ centers, whereas the diffraction-limited image was able to control only two NVs. It has been determined that the STED beam can preserve the NV spin state in Rabi oscillation if the STED beam does not start to populate the MS state. Rabi oscillation¹¹³ can be performed with subdiffraction spin localization, whereas the effect of the STED beam induced a loss of information in the phase of the spin state when applying the Hahn-echo sequence, showing that quantum sensing is limited in STED high power operation. This was attributed to the different zero-field splitting of the ground and ESs; when a STED beam is applied and NV is forced to the ES, even if it is then de-excited, it experiences different coupling with external spins, as it has acquired a phase caused by the coupling of the ES, breaking the symmetry of the Hahn-echo sequence. Due to the high refractive index of diamond (2.4) and Mie-scattering resonances in NDs, a limit was believed to exist for STED to image multiple NV centers in NDs; thus, it was shown that STED can be used to distinguish multiple nanometric distant NV centers in 40- to 250-nm-sized NDs with a resolution of 10 nm.¹¹⁴ In Figs. 3(a)–3(e), multiple NV centers in 100 nm NDs are shown using STED, and their image is correlated with SEM images and with their ODMR spectra. This result also proved the possibility of attributing a

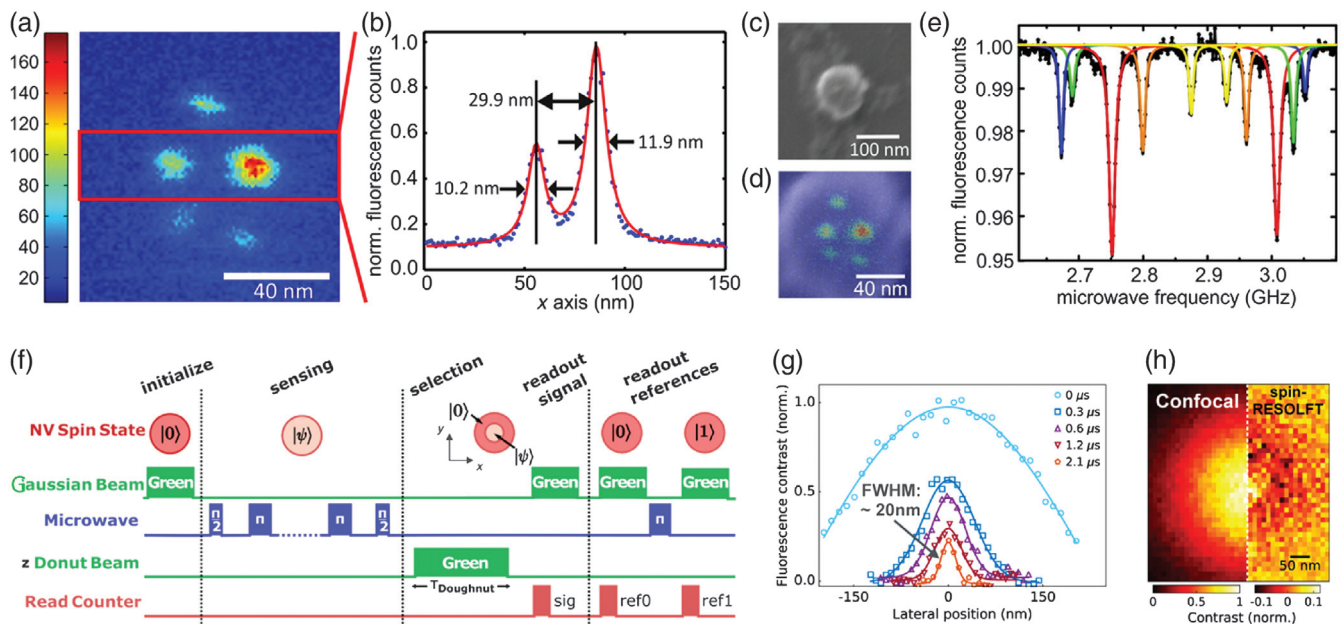


Fig. 3 Spin-STED applied to multiple isolated NV⁻ centers in 100 nm ND. (a) Subdiffraction image of five isolated NV centers in a single ND. (b) Vertical STED image profiles as indicated in (a). (c) SEM image of the same ND with (d) the overlay of the STED image. (e) ODMR spectrum of the same NV centers in the same ND showing distinct frequency pairs corresponding to the five NV centers. Reproduced with permission from Ref. 114, © 2013 American Chemical Society (ACS). (f) Spin-RESOLFT experimental sequence combined with AC magnetometry with the dynamical decoupling pulse sequence for quantum sensing using NV centers in diamond. (g) Spin-RESOLFT profiles for a single NV center and different doughnut beam duration with a power of 700 μ W. (h) Spin-RESOLFT image of the same NV as in (g) with similar resolution of \approx 35 nm but with 25 μ W power and a longer duration of 50 μ s. Images reproduced from Ref. 115, © 2017 OSA.

spin transition to each NV in the ND, opening the door for studies of fundamental spin-spin interaction of NV in NDs, for example, collective emission. While spin-STED has never been applied for biomedical imaging due to the high energy used, its current area of application is in NV centers fabrication with nm precision/localization. In this space, only a few examples of spin-STED use can be found. For scalable architecture, for example, in quantum technology using spin qubits, quantum photonics, and quantum sensing, the fabrication of an array of NV⁻ centers is required. Here, there is a need for two conditions to be simultaneously achieved, which are the accurate positioning of the NV centers and its high probability of creation. Using few keV ions energy, it is possible to achieve a positioning accuracy of NV in the nanometer range, with, however, a low yield in the few percent of conversion of nitrogen to NV centers after annealing. STED can be used to assess implantation/detection technology of single implanted atoms as an example⁶⁰ to determine the spatial accuracy of NV implantation and yield. However, so far, STED for NV fabrication has not been widely used. Nanoscale site selective magnetic sensing of 1 × 4 arrays of NV sites with a 60 nm diameter and 100 nm spacing was achieved using STED imaging.¹¹⁶

3.2 Spin-Reversible Saturable Optical Fluorescence Transitions

RESOLFT is a variant of STED, where fluorescence depletion occurs via an MS or intersystem crossing state. The MS state is required to have a long lifetime. In general, RESOLFT requires lower power than the STED beam, as such, it is easier to apply the process that can be affected by high laser intensity, specifically in biological samples, where phototoxicity is a major issue in live imaging.¹¹⁷ Spin-RESOLFT is thus another variant of spin-STED or RESOLFT when applied to NV⁻ centers in diamond⁴⁶ for achieving super-resolution of the spin localization. Spin-RESOLFT is thus a deterministic superresolution method providing targeted probing of individual NV spins with nanometric resolution well suited for coherent nanoscale AC magnetometry. Due to the involvement of the long-lived MS state and the lower intensity, compared with STED, it has the potential to achieve coherent manipulation of NV spins using complex spin sequences with simultaneous superresolution imaging of the NV position, without disturbing the phase of the surrounding spins and thus achieving nano MRI with subdiffraction localization.

NV⁻ undergoes the transition to the nonspin selective MS state for spin numbers of ±1, inducing fluorescence reduction. Spin-RESOLFT has been implemented by illuminating the sample with a sequence of a Gaussian 532-nm pulsed laser to polarize the NV⁻ spins in the $m_s = 0$ GS, whereas a microwave pulse excites the spin to the state $m_s = ±1$, and another doughnut-shaped green laser selectively allows us to manipulate the spin only in the central part of the beam, achieving subdiffraction spin manipulation of NV⁻ centers. The technique resolution is given as

$$d \approx \frac{\lambda}{2 \times \text{NA} \times \sqrt{1 + \Gamma \tau_D}}, \quad (2)$$

where Γ is the rate of optical excitation of the spin, and τ_D is the duration of the doughnut beam that is only limited by the spin-state relaxation time (>100 ms) and the optical transition

lifetime $\tau_{fl} \approx 12$ ns (this is instead of limiting STED resolution). The advantage compared with spin-STED is the reduced power at the sub-mW level, which is four orders of magnitude lower than STED, while achieving the same resolution.¹¹⁵ Due to the lower power used in this method, spin manipulation based on Rabi oscillations and spin-echo measurements could be performed with spatial selectivity locating 150 nm apart NVs centers. This enabled the study of the spin coherence times of closely NVs to determine the content of magnetic impurities in the local nanoenvironment. Spin-RESOLFT microscopy can enable precise nanoscale mapping of magnetic field patterns with a shown resolution as low as ≈ 20 nm, using a lower power depletion beam. In particular, mapping of the nuclear spins exterior to the diamond was achieved and imaged with 50 nm lateral resolution. The proton NMR line-width was not degraded by the scanning laser beam,¹¹⁵ showing promise for NMR signals detection of nuclear spins with high spatial localization. In Figs. 3(f)–3(h), a scheme of spin-RESOLFT combined with a quantum sensing sequence (XY8-k dynamical decoupling pulse sequence) is achieved in bulk diamond with 20 nm resolution. A spin-RESOLFT magnetic imaging sensitivity of 250 nT/ $\sqrt{\text{Hz}}$ was achieved with a resolution of 50 nm (whereas on the confocal mode, the sensitivity is of 60 nT/ $\sqrt{\text{Hz}}$), as the resolution is increased by longer duration of the doughnut laser beam, which in turn reduces the sensitivity. As such spin-RESOLFT based on diamond CCs may be more applicable to biology and quantum sensing than all the techniques described so far.

4 Ground-State Depletion Microscopy, Metastable-State Depletion Microscopy, and Structured Illumination Microscopy

In the GSD microscopy method, the NV GS is depleted by shelving the emitter in the ES. A high-intensity 532 nm excitation beam has a doughnut shape and is used to force the NV in its ES, whereas NV emission occurs in all of the samples except in the dark center. The location of closely packed NVs is observed as nanosized dark spots in a larger bright area. The localization below the diffraction limit corresponds to a dark point.³¹ Imaging was achieved with this approach in diamond due to low photobleaching at high-intensity beams. Mathematical deconvolution postprocessing algorithms using the effective calculated PSF are used to obtain the positive image. With this method, a resolution of 8 nm with several GW/cm² in a low-density NV sample of an optical grade bulk diamond has been obtained. The direct super-resolved image could be obtained using an excitation Gaussian beam modulated at 1 kHz and, at 561 nm, used to excite the fluorescence of the NVs located at the doughnut minimum that remained dark, as in the GS. With the direct GSD methods, 14 nm resolution was achieved, and NVs 17 nm apart were located in the sample. A variant of GSD has been demonstrated via shelving in the MS state,⁶¹ as it had been initially proposed.⁸⁹ A long-lived MS state is required. A red laser at 638 nm excites the NV center and efficiently transfers it to an MS dark state, while the dark state is emptied by blue light (479 nm) back to the ES, thereby depleting its GS. A resolution of 16 nm was achieved with 5 mW power. It is understood that GSD via the dark state can be sample dependent, where high nitrogen doping is necessary to avoid conversion of the NV⁻ from the negative to the neutral

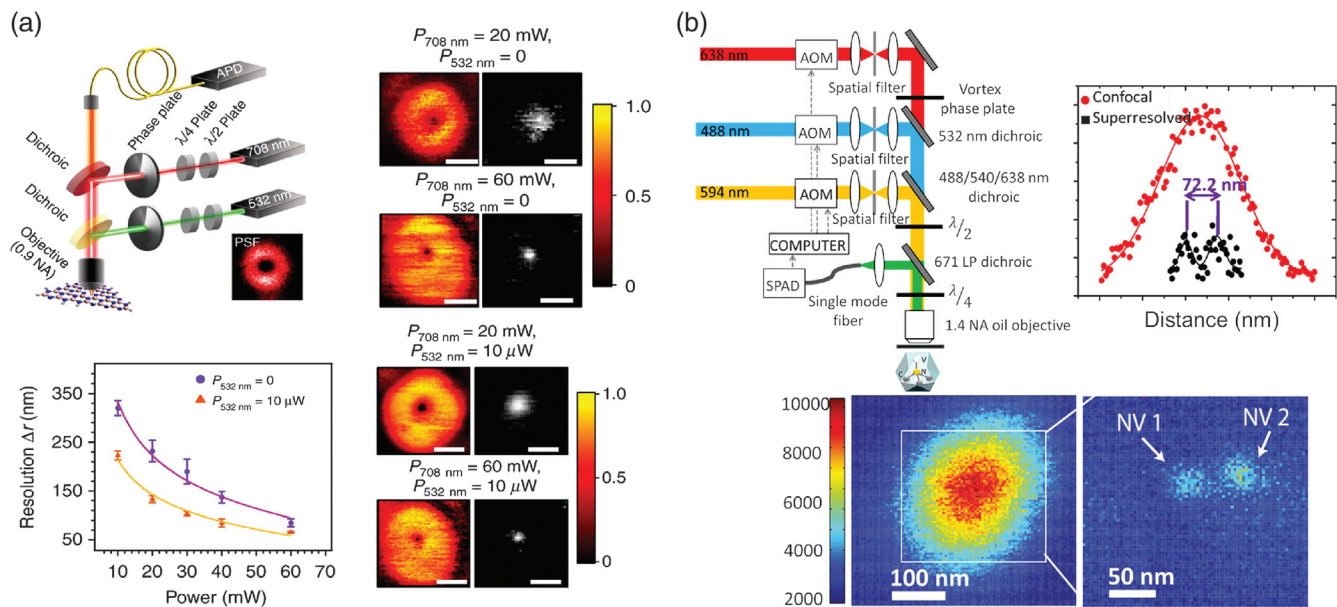


Fig. 4 (a) Schematic of the experimental conditions used to perform GSD nanoscopy applied to hBN flakes with one or two excitation lasers with doughnut-shaped intensity profiles. Here, 532 nm is used as a repumping laser. The direct images and deconvoluted ones are shown in the presence of only the 532-nm or both 532- and 708-nm lasers, together with the resolution achieved, showing an improved resolution in the presence of the two lasers. Images reproduced from Ref. 119, Creative Commons BY license. (b) Schematic representation of GSD microscopy applied to NV⁻ in NDs. Three lasers operating at the wavelengths of 488, 594, and 638 nm are used. The 638-nm laser has a doughnut-shaped intensity profile and switches off the center via the MS state, while the 488-nm laser is a reset beam used to repopulate the ES. Confocal and super-resolved images of 2 NV⁻ at 72-nm distance in the same ND. A single NV⁻ was resolved with 36 nm. Images reproduced from Ref. 118, Creative Commons BY license.

charge state. Compared with STED, as this method involves a long-lived MS state, it requires a lower power, also in comparison to the GSD via the ES. This method has never been applied in spin manipulation, and it has been referred to in recent literature to be a CSD method, involving the NV charge state conversion from a negative to a neutral state. GSD microscopy using the MS state has been applied to NDs,¹¹⁸ where the charge conversion of the NV⁻ was not observed due to the high concentration of nitrogen in the NDs. Here, three beams were used: a probe beam at 594 nm, a depletion beam at 638 nm, and a reset beam at 488 nm. The depletion beam at 638 nm shelves the NV⁻ centers to the MS dark state everywhere except in the local minimum, whereas a Gaussian beam at 594 nm probes the NV⁻ centers, and a 488-nm reset beam is used to repopulate the ES. Super-resolution imaging of a single NV⁻ center with an FWHM of 36 nm is demonstrated, and two nearby NV⁻ centers were resolved with 72-nm separation, as shown in Fig. 4(b). GSD microscopy applied to NV⁻ in NDs requires a much lower optical power compared with the bulk diamond previously reported. However, this work further evidences the need to control the NDs nitrogen concentration to better tailor the NV photophysics as an example to separate the charge conversion possibility and combine GSD in NDs with spin control. So far, GSD has not been applied in spin manipulation.

A variant of GSD microscopy was applied to a class of quantum emitters with a zero phonon line (ZPL) at 778 nm in 2D

hBN¹¹⁹ [Fig. 4(a)]. Here, complex photophysics of a four-level system is assigned to the photon-correlation dynamics of the emitters under different laser excitation wavelengths, where it is found that 675-nm (or 708-nm) excitation induces a transition to a dark state (possibly a different charge state) through the long-lived MS state; while combining the 708-nm with a 532-nm excitation, the emitter is repumped in the ES, inhibiting the otherwise faster nonradiative decay from the intermediate to the GS. As such, by combining GSD with two excitation beams, a resolution of 62 nm was achieved with a lower power compared with a single beam GSD. This method could also be associated with a charge state conversion. No CCs GSD microscopy has been used in the cellular environment so far due to the high energy used. Structured illumination (SIM) has been compared to STED side-by-side using NV centers in 35-nm FNDs and bulk diamond material. It has been shown that STED provides more structural details, whereas SIM provides a larger field of view with a higher imaging speed. SIM has been compared also with wide-field imaging, as it is expected to have a factor of 2 resolution improvement, and, using NV centers in FNDs, the achieved resolution was ≈ 304 and ≈ 131 nm, respectively.¹²⁰ While this is not the ultimate resolution of SIM with FNDs, SIM has found many applications in biological science, where less resolution is needed, and it is not excluded that such large FNDs could find better applications in SIM rather than STED.

5 Single Molecules Location Microscopy and Spin-SMLM

SRM techniques can use statistical intensity switching due to the fluorescence intermittency of the fluorescent nanoprobe in the entire field of view of a wide-field microscope. Using single emitters localization imaging reconstruction algorithms, the precise locations of the probes surrounding sub-100 nm features of the object to image can be achieved. SMLM is the general term used to group all of the techniques based on this approach. SMLM methods are implemented on a wide-field microscope using an electron-multiplying charge-coupled device camera with sensitivity of single photons detection being possible. Sequences from 100 to 10,000 individual camera frames are taken, and each frame is imaging only a limited number of different subsets of individual isolated fluorescent nanoprobe each time, which is accidentally switched on for each subsequent camera frame. The image with sub-100 nm resolution is reconstructed by determining the spatial positions of the individual fluorescent molecules from their intensity intermittency in these many camera frames. Deconvolution of the single emitters PSF is achieved. SMLM relies upon the presence of a high density of single emitters, which can be switched on and off within a time frame of 10 to 100 ms. Different fluorophores photophysics are used to achieve their stochastic on-off switching, and this differentiates various methods. PALM employs the excitation laser wavelength-dependent fluorescence activation of the so-called “photo-activable” fluorescent labels, which are brought to an “on” state by the laser excitation; after activation, these fluorophores emissions subsequently photobleach. Specifically, PALM uses photoactivable green fluorescent proteins as labels, which are genetically engineered fluorescent proteins. Instead, STORM originally utilized stochastic fluorescence transitions of organic dye. These methods can achieve higher resolution (10 to 20 nm) than STED with much lower power and, as such, lower phototoxicity than the other deterministic methods; however, at the expense of longer acquisition time of many frames, they are thus less applicable to *in vivo* imaging. SMLM high spatial resolution (10 to 20 nm) is achieved at the expense of low time resolution, usually from a few to several seconds. It has been improved to reach 0.5 s using single excitation in 2D imaging in the cell environment¹²¹ with a reduced spatial resolution of 25 nm; whereas, time resolution of 1 to 2 s is needed to achieve a 3D spatial resolution of 30 nm in the lateral directions and 50 nm in the axial direction. The long acquisition time can introduce drift, requiring fiducial markers and correction to avoid image artifact. More importantly, long acquisition times introduce an upper limit to the time resolution and speed when it is needed to resolve live-cell dynamics or to achieve real-time imaging of subcellular components. Various deconvolution and machine learning algorithms can accelerate PALM and STORM as an example, using deep learning methods;¹²² however, these techniques are not yet commonly applied, even if they are very promising. The localization of the emitters in SMLM is given as

$$\Delta_{\text{loc}} \approx \frac{\Delta}{\sqrt{N}}, \quad (3)$$

where Δ is the FWHM of the PSF (resolution) of the single emitter, and N is the photon count. The technique is only limited by the number of photon counts associated with the single

emitters. As such, bright single emitters with fast switching from the bright and dark state can provide very high localization and resolution.

Several fluorescent labels have been used for SMLM as described above: organic molecules have the smallest size, and the excellent blinking properties are, however, generally dim and undergo rapid photobleaching; photoactivable or photoswitchable fluorescent proteins suffer from poor localization precision and low photon counts. Nanomaterials, such as QDs, carbon dots, polymers dots, and silica NPs, have been used, showing promising results due to their high brightness and photostability. Nanomaterial limitations can be found in their phototoxicity or their large size compared with organic molecules.¹²³ Among these nanoprobe, NDs have been also used.

SMLM has been applied to NV centers in NDs³³ based on the blinking behavior of NV⁻ photoluminescence due to the surface defects and electron tunneling to near-surface defects, achieving a resolution of 20 nm and being able to discern two NVs in a single ND 20 nm apart. A STORM microscope enhanced by spin manipulation was achieved in bulk diamond using the photoionization of NV⁻ to its NV⁰ for single sparse NVs, achieving a super-resolution of 27 nm with the spin manipulation and magnetic field sensitivity of 190 $\mu\text{T}/\sqrt{\text{Hz}}$.⁴⁷ SMLM based on NV in diamond and NDs can permit parallel magnetic imaging with nanoscale resolution. However, the photophysics of NV⁻ are due to the low nitrogen concentration bulk diamond, which also has a limited number of naturally occurring NV centers, reducing the possibility of reconstructing the image of nanometric size samples. SMLM in NDs has further been implemented to achieve spin manipulation with subnanometer resolution in NDs,⁴⁸ permitting also the improvement of the super-resolved images of collective blinking NV⁻ centers to 23 nm (otherwise of 50 nm). By labeling cells bound to iron oxide magnetic NPs with biotinylated 70 nm FNDs, the nanoscale magnetic field optical images with 17 nm resolution within the cells were achieved using the spin-SMLM method⁴⁹ and magnetic field sensitivity of 85 nT/ $\sqrt{\text{Hz}}$, as 1000 NVs were present in a single FND rather than 1 NV. This is the first application of the spin-SRM method to the cells' environments. One limitation for *in vivo* imaging with this technique is the longer acquisition time, which could be improved using deep learning methods.¹²⁴ SMLM and its spin variant using NDs have more potential for biomedical applications if smaller NDs with bright NV centers could be available, while, at the moment, large NDs of 35 to 70 nm have been used. An improvement of the NDs material to achieve better applicability of these techniques is expected, for example, with lower nitrogen content for improved quantum sensing combined with parallel super-resolution imaging.^{125–127}

Using quantum spin control, super-resolution localization of NV⁻ centers in diamond with localization better than 1.4 nm was achieved with subnanometric resolution. Here, a scanning confocal microscope and quantum-controlled photoswitching were used.¹²⁸ Photo-switching is realized by encoding the spin quantum phase using a pulsed magnetic field gradient. This method can find applications in addressing and controlling coupled qubits spins in diamonds.

Other CCs in solid-state nanoscale materials are emerging as probes for SMLM. SMLM has been applied to quantum emitters in a monolayer of hBN.¹²⁹ The mechanism is attributed to the CCs photoswitching after exposure to a 561-nm laser due to possible photo-induced ionization and recombination of defects, revealed by correlated TEM imaging, such as boron vacancy

(V_B), and switching between its neutral and negative charged states. Here, the super-resolved images of 46 nm were achieved with the possibility of locating quantum emitters 11 nm apart. This technique is relevant to increase the understanding of quantum emitters in 2D materials. By combining SMLM and

spectroscopy, the spatial and spectral correlation of quantum emitters in chemical vapor deposition (CVD) and exfoliated flakes of 2D hBN was shown,¹³⁰ where two types and one type of defects were identified in the respective material [Fig. 5(c)]. These results align with recent findings of the origin of the

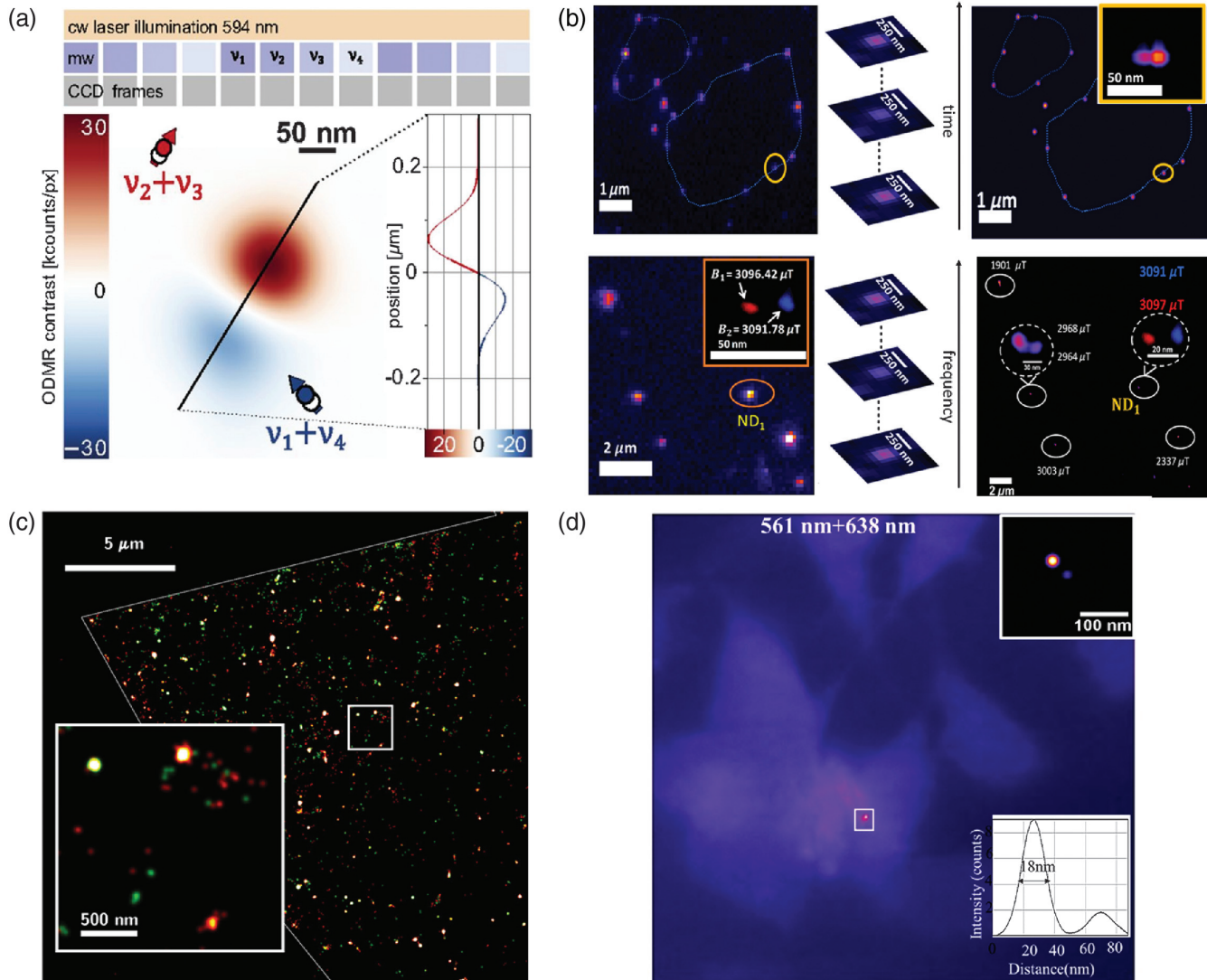


Fig. 5 (a) Spin STORM applied to NV⁻ center in bulk diamond. STORM-ODMR measurement sequence under a 594-nm excitation laser to induce photoionization of the center into its neutral charge state, combined with a scanning of the microwave frequency for each widefield frame. Sensing of two NV⁻ centers is shown with a nanometric localization and STORM-ODMR image. The zero-crossing (line scan) between both centers shows mutual distances of the centers below the STORM resolution. Image reproduced from Ref. 47. (b) Nanoscale magnetic field optical images of labeled cells bound to iron oxide magnetic NPs with biotinylated 70 nm NDs. Upper figures showing super-resolution only based on SMLM using 561 nm and lower figures showing magnetic field sensing and localization combining ODMR information achieved by a microwave frequency scan. Reproduced from Ref. 49, with permission from the Royal Society of Chemistry. (c) Super-resolved image of hBN flakes resolving the different types of emitters (green and red) based on photoswitching of the V_B charge states and other emitters in the 2 to 2.2 eV spectral region. Reprinted with permission from Ref. 130, © 2019 ACS. (d) SMLM applied to 4H-SiC NPs of 40 nm after cell incubation achieving 18 nm in the cellular environment. The SiC NPs revealed the presence of multiemitters in the same NP with SMLM using different excitation wavelengths at 561 and 638 nm. Image reproduced from Ref. 59, © 2020 American Physical Society (APS).

quantum emitters in exfoliated flakes of hBN attributed to $V_B C_N$ concerning visible emitters and the V_B in the neutral or negative charge states. The SMLM technique was also applied to investigate the optical properties of single-digit hBN NPs (3.0 ± 0.7 nm) produced by cryogenic exfoliation.¹³¹ hBN NPs/nanoflakes due to their size properties can be applied for bioimaging and sensing applications in combination with SMLM, GSD, or RESOLFT microscopy; however, so far, no applications in biological samples imaging have been shown. SMLM in hBN has been performed to achieve information about the origin of the emitters, which is often not fully understood.

While hBN emitters have recently shown the possibility of having an ODMR signal¹⁸⁶ concerning the negative charge state of V_B^- with a coherence time of $2 \mu\text{s}$ at room temperature, its application to spin-SMLM has not been shown yet, possibly due to its central wavelength of 850 nm when excited at 532 nm. This emitter has not yet been isolated as a single emitter. The V_B^- has been determined to be the dark state of the $V_B H$ used in a recent demonstration of SMLM¹³² of hBN samples in air and acidic solutions. The presence of water increases the conversion into the visible luminescent neutral charge state. A recent review on the potentials of hBN in SRM and the photo-physics of CCs involved can be found in Ref. 26.

SMLM was used to study the blinking properties of quantum emitters in bulk SiC and NPs sized from 8 to 100 nm¹⁵ of different SiC polytypes, showing a resolution dependent on the NPs size and excitation wavelength.⁵⁹ A resolution of 20 nm and a minimum distance between single emitters of 40 nm were observed, even with the uptake of the SiC NPs in the cellular environment of MCF10A cells [Fig. 5(d)], showing the potential of these nanoprobe as biomarkers. Using single digit (3 nm) SiC NPs with the ODMR emitters signature,⁷⁸ spin nanoscopy using dual-color excitation could also be achieved as the red (CAV) and NIR (DV) CCs are present in the same NPs. As SiC NPs can reach the size of 1 to 1.5 nm, comparable with those of pores in the cellular membrane,²³ and their biocompatibility has been demonstrated¹³³; the combination of 3-nm NPs with CCs with optical spin readout may be the solution to the large FNDs applicability to spin-SRM. However, spin-SMLM has not yet been demonstrated, as the quantum emitters are in the infrared (900 and 1100 nm), where commercial systems do not operate, as well as the conventional detectors' efficiency is much lower.

6 Two-Photon Microscopy

Two-photon microscopy (2PM) is used to increase the resolution along the optical axis of the microscope, which is generally much worse compared with lateral resolution for any fluorescent microscopy method. Its main application is deep tissue imaging,¹³⁴ as by exciting with two photons at a longer wavelength (generally in the infrared) scattering and background are reduced. Combined with adaptive optics to correct the optical aberration within the sample limiting resolution, it can provide SRM in 3D.¹³⁵ 2PM has been applied first to diamond bulk material¹³⁶ using 1064 nm and showing it is possible to excite NV in the same way as using SP absorption with 532 nm, showing similar photostability with high power excitation. Application to micron-sized diamonds with NV centers has followed,¹³⁷ with FNDs for their characterization of high brightness due to many NV centers being created within the NDs,¹³⁸ then for drug delivery,¹³⁹ and in living cells.¹⁴⁰ 2PM, however, does not provide SRM by itself, but can be combined with SRM to achieve better resolution in the z direction. It can be used to

image the localization of the production of NV centers with depth in bulk diamond.¹⁴¹ 2PM has then been implemented in 5- to 100-nm NDs in combination with adaptive optics and super-resolution radial fluctuations algorithms,^{142,143} achieving 43-nm resolution. This is a freely available plug-in module for ImageJ, which requires a minimum of 100 frames of confocal images. Super-resolution radial fluctuations make use of the fluctuations in the radial symmetry measured over a large number of images of the same object to extract super-resolution images, and it is a computational method.¹⁴⁴ 2P microscopy has also been successfully applied to ≈ 200 -nm hBN flakes using a ps-pulsed laser at 708 nm.¹⁴⁵ No applications of 2PM in combination with SRM using CCs in the cellular environment have been shown.

7 Charge-State Depletion Microscopy

As previously mentioned, the NV center in diamond, like many other CCs, occurs in two fluorescent charged states: neutrally charged NV^0 and negatively charged NV^- . Their well-known studied ZPLs are at 575 and 637 nm, respectively. The presence of one or the other charge state is dependent on the nitrogen doping concentration of the starting material (the presence of substitutional nitrogen center P1) in both bulk and NDs.¹⁴⁶ In low nitrogen concentration of diamond with different excitation conditions, the two charged states can transform from one to the other, known as the photochromic effect.^{147,148} Only the NV^- electron spin GS can be optically initialized and detected, whereas the NV^0 charge state does not exhibit such properties ($S = 1/2$). They are both very photostable once the charge state is controlled. It is understood that high nitrogen doping can stabilize the charge state of the NV^- .¹⁴⁹ On the other hand, a high nitrogen concentration is the main source of the reduced coherence time of the NV^- .¹⁵⁰ The charge state conversion process of the NV center excited by visible light has been demonstrated to be a two-photon process, increasing quadratically with the optical field intensity.¹⁴⁸ CSD microscopy³⁵ relies on using a 637-nm laser to convert the NV^- into the NV^0 , and a 532-nm laser converts it back or initializes the NV^- , achieving a resolution of 4.1 nm by optimizing the laser pulse sequences. The method is not deterministic, as the conversion rate of the charge state for NV^- is around 75%, and this is a limitation of the technique. In CSD nanoscopy, three lasers are applied in sequence: the NV centers at the focal point of a Gaussian beam are initialized to NV^- by a 532-nm laser beam, and a doughnut-shaped 637-nm laser beam is applied to convert the charge state to NV^0 , except for the NV centers at exactly the center of the doughnut-shaped beam. The third laser at 589 nm is nondestructively used to read out the NV charge state, as it can efficiently pump the spontaneous emission of NV^- centers without changing its charge state. Only the NV centers at the 637-nm laser beam center will be bright in the image under 589-nm excitation. The resolution of CSD nanoscopy can be increased by increasing the power and duration of the doughnut-shaped depletion-laser beam. The electron spin-state dynamics of adjacent NV^- centers can also be controlled via the CSD. Using ODMR CSD and Rabi oscillation with CSD, two 100-nm distant NV^- spin states, with the same resonant microwave frequency, were individually controlled.³⁵ Here, the CSD method is not influencing nearby spins, as the method is based on charge state conversion, and, as such, when NV is in the neutral charge state, it is not influenced by the microwave. CSD and its spin variant have been applied to ultrapure diamond, with 500-ppb nitrogen

concentration, and, as such, this method also appears to be material doping dependent. CSD microscopy has been applied to an ensemble of NV centers in bulk diamond with 6.1-nm resolution.¹⁵¹ Using an NIR laser (780 nm), the charge-state conversion rate was improved in CSD.¹⁵² Using picosecond lasers and a low repetition rate, a resolution of 12 nm was achieved with 1-mW depletion power, bringing the technique among the lowest power high-resolution methods.¹⁵³ The resolution of the technique can be increased by a longer depletion beam pulse and higher power. Super-resolution multifunctional sensing has been shown using low-power CSD nanoscopy of arrays of high-density NV centers used as local electromagnetic field sensors for local density of states and electrical conduction with a resolution of ~ 49 nm.¹⁵⁴ The methods regardless of the low power have never been applied to biological samples, mainly because they have never been applied to NDs or FNDs as of yet, possibly due to the high nitrogen concentration of the NDs.

8 Quantum Methods

While the previously described methods rely on nonlinear optics effects or nonstationary emission of fluorescent markers for overcoming the diffraction barrier, which is due to stationary and linear classical optics, an alternative approach is based on resorting to quantum optics. High-order quantum interference patterns arising in quantum optics can yield spatial distribution of correlations much denser than what is classically allowed. Using nonclassical light as the source of illumination, subshot noise measurement can be achieved in virtue of quantum entanglement; the techniques are known as quantum illumination,¹⁵⁵ which permits us to achieve imaging in the presence of noisy low illumination conditions, while they do not provide super-resolution. Various methods to achieve high sensitivity, image contrast, and, to a certain extent, resolution enhancement via quantum optics have been based on illuminating an object with nonclassical light, such as squeezed light, SP emitters, or entangled photons.¹⁵⁶ Another proposal was based on using samples that emit multiphotons while being illuminated by classical light. By using coincidence measurements, the diffraction limit can be defeated.¹⁵⁷ However, no samples can currently emit photon pairs or multiple photons. As such, an alternative to Hell's proposal is to use higher-order correlation methods¹⁵⁸ in the specific SP emitters.

8.1 Single Photon Second and Higher Correlation Methods

Photon antibunching¹⁵⁹ is observed in most common fluorophores, such as organic dyes, QDs, and CCs, in wide-bandgap materials even at room temperature. For these emitters, the photons have sub-Poissonian statistics, which consist of the suppression of emission of two photons at the same time. Therefore, simultaneously detected pairs of photons from such fluorophores provide information of the number of emitters; if N emitters are measured, their zero delays ($\tau = 0$) second-order photon correlation is $g^{(2)}(\tau = 0) = 1 - \frac{1}{N}$. The same quantum emitters are widely used in traditional nonlinear and nonstationary SRM, as described in previous sections, via spontaneous emission. Because of photon antibunching, a scanning fluorescence microscope spatial points in the image are, in principle, based on sub-Poissonian photon statistics, where the number of simultaneous multiphoton detection events is much smaller than it is for classical light for any order. Performing an N -photon

coincidence measurement is equivalent to measuring N -photon, narrowing the effective PSF by a factor of \sqrt{N} .¹⁶⁰ The PSF is, in this case, the probability of detecting a photon at the position x , $P(x)$, where the probability of detecting N photons at x is narrower, $P(x)^N$, so the FWHM reduces by \sqrt{N} . The first experimental demonstration was based on CdSe/CdS/ZnS colloidal QDs photon antibunching in the image plane of a wide-field fluorescence microscope, determining the spatial distribution of missing two- and three-photon coincidence events and reconstructing second- and third-order super-resolved images.⁵⁴ This method resembles super-resolution optical fluctuation imaging (SOFI),¹⁶¹ as intensity correlations are detected in the image plane of a fluorescence microscope. However, in SOFI, the fluorophore brightness fluctuations provide super-Poissonian photon statistics, whereas quantum SRM antibunching of photon emission is a sub-Poissonian statistic. Super-Poissonian photon statistics are highly dependent on the specific emission fluctuations of the fluorophores, while antibunching is a universal subshot statistic. Antibunching imaging is limited by the SP detector technologies background noise and, by their point detectors nature, responsible for a small fill factor.¹⁶² The method has been applied to NV in electronic grade bulk diamond,⁵⁵ where second- and third-order photon correlation functions, $g^{(2)}(0)$, $g^{(3)}(0)$ maps, were obtained and deconvolved to determine the PSF, $P(x)$, to reconstruct the super-resolved images [Figs. 6(a)–6(e)]. Here, a confocal setup with single-photon avalanche photodiodes (SPADs) and photon correlation electronics was used. An FWHM of 290 nm was achieved to resolve the location of 3 NV centers with 2 NVs at 270 nm apart [Fig. 6(e)]. The localization and super-resolution are limited to the third order, with a factor of $\sqrt{3} = 1.73$ improvement. The method appears very far from the current resolution and localization obtained from STED or SMLM, and it is unclear if it can be applied in a higher density of NV centers as in optical grade diamond or NDs due to the presence of high background and multiple CCs in the same ND, in addition to collective emission effects observed.⁴⁸ Further, the time acquisition to achieve a higher-order correlation function and the complexity to implement higher-order correlation using single SPADs could be a limit to improving the current resolution.

8.2 Quantum Enhanced SRM

Quantum correlation methods have shown the possibility to be improved by adopting image scanning microscopy (ISM), which makes use of a fiber bundle in place of the confocal pinhole and on a small array of faster SPADs, offering a twofold enhancement in resolution compared with a traditional wide-field or scanning confocal microscope.¹⁶⁵ In particular, ISM has been proposed as a method in traditional SRM that could be implemented together with the quantum correlation of single emitters, as shown by quantum image scanning microscopy (Q-ISM) [Figs. 6(f)–6(h)].^{57,163} This is because in ISM each pixel in a detector array acts as a small pinhole in a confocal laser-scanning microscope,¹⁶⁶ which can be further improved using a recently developed array of SPADs.¹⁶² In addition, by adopting ISM, SMLM could also be equipped with quantum correlation functionalities. First, it has been shown how the quantum correlation could be applied to SMLM implemented by a fiber bundle camera.¹⁶³ Here, the SMLM localization principle is implemented using high quantum efficiency, low noise, scalable architecture group of SPADs, where the fill factor is improved

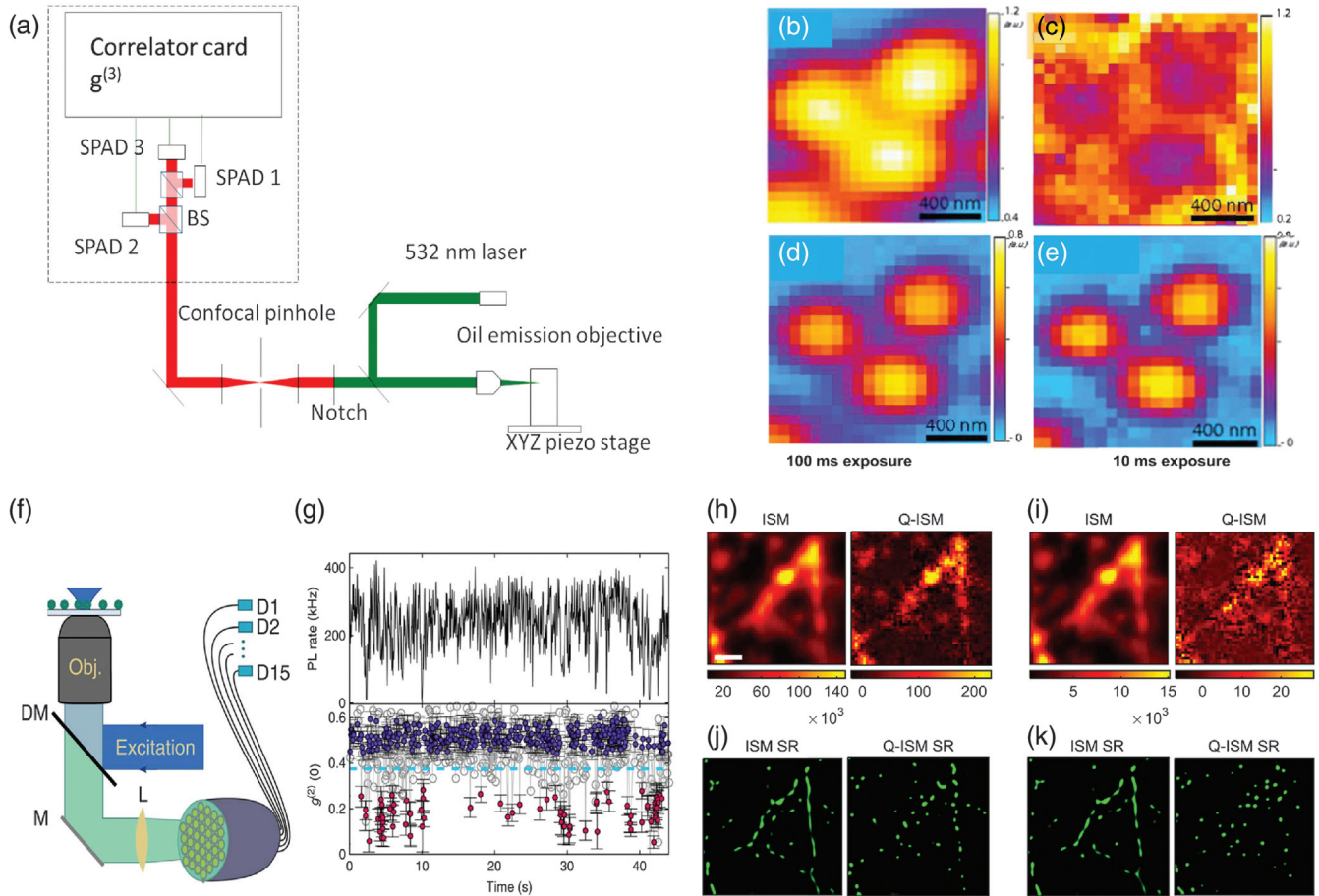


Fig. 6 (a) Schematic of a confocal laser scanning microscope equipped with SPADs and a third-order correlation electronics. (b) Diffraction-limited image from the confocal point of three NV centers in bulk diamond. (c) Map of the $g^{(2)}$ function and super-resolved images using the quantum correlation information after using a quantum reconstruction algorithm for (d) the second-order and (e) third-order. (b)–(e) Images are reproduced with permission from Ref. 55, © 2014 APS. (f) Schematic of an SP fiber bundle camera with 15 SPADs. (g) Photon count time trace (top) and quantum correlation (bottom) for two QDs. Blinking of one QD is followed by antibunching, $g^{(2)}(0) \approx 0$, in red. Blue circles correspond to the case of more than one emitter blinking, while gray circles correspond to insufficient statistics. Images (f) and (g) are reproduced from Ref. 163, Creative Commons BY license. (h), (i) Images of microtubules in a fixed 3T3 cell labeled with QDs imaged using ISM and Q-ISM and corresponding SR images (j), (k) for 100 ms and 10 ms acquisition times; the scale bar is 500 nm. Images (h)–(k) are from Ref. 164, © 2019 OSA.

using the fiber bundle. The time traces of single QDs count rates are acquired with the second-order photon correlation function $g^{(2)}(t)$ [Fig. 6(g)] and analyzed in time bins of 0.1 s. Single-emitter localization is achieved, postselecting only single emitters based on the values of $g^{(2)}(0) < 0.375$ with localization of 20 nm on a single emitter, which is comparable with SMLM in the widefield imaging mode. Tracking of single and two emitters separated by 100 nm was achieved with this method. Both localization and tracking are not currently superior to traditional SMLM due to the small field of view. This method, however, provides a solution to the current SMLM, requiring a sparse number of single emitters to avoid multiemitters in the diffraction spots (which generally require many camera frames), and, also, it relies less on the fluorophores photoswitching underlying mechanism, as it can be applied also to photostable single

emitters. This method permits the rejection of multiemitters from the quantum correlation measurements or the use of multiemitters fitting algorithms. The approach can be scaled up by SPAD arrays to achieve faster antibunching maps.¹⁶² In addition, faster blinking emitters could be used to increase the occurrence of single-emitter events and localizations of three emitters or more. As such, scalability of this method still relies on a photo-switching mechanism. If compared with SMLM traditional methods for both localization and tracking, in quantum-enhanced SMLM, it is not clear if outstanding problems in SMLM, such as limited speed due to acquisition of many camera frames, can be surpassed, as the antibunching acquisition can slow down this method as well. Localization precision below 30 nm or better has been theoretically predicted using antibunching and photoswitching (quantum-optimally enhanced

STORM) of multiple emitters, even when closely spaced (125 emitters per μm).⁵⁶ Super-resolution Q-ISM has recently proved an increase in the resolution of confocal scanning microscopy up to twofold, and it has been applied to microtubules of fixed 3T3 cells labeled with QDs.⁵⁷ Images of the microtubules with confocal scanning microscopy, ISM, and Q-ISM are compared.⁵⁷ The resolution enhancement factors compared with the wide-field image are 1.29 and 1.74 for the ISM and Q-ISM, respectively, for the image of single QD. The use of nanosecond response time SPADs permits the improvement of the signal-to-noise ratio. Using Fourier reweighted¹⁶⁵ Q-ISM, further resolution improvement of 2.34 was achieved. The acquisition time to achieve a high signal-to-noise ratio in a Q-ISM image is generally longer than that for an ISM image, of the order of tens of milliseconds per scan step. As such, joint reconstruction of the images of the two methods was implemented via sparse reconstruction (SR) algorithms, and images of fluorescent QDs were validated via correlative electron microscope measurements.¹⁶⁴ In Figs. 6(h)–6(k), images from ISM and Q-ISM and their SR of fixed 3T3 cells labeled with fluorescent QDs with different dwell times are shown, providing a relatively accurate reconstruction of the images with 10 ms exposure time.

Another quantum correlation-enhanced microscopy approach to defeat the diffraction limit has been proposed theoretically. It has been proposed to combine quantum correlation and structured illumination (SIM) to achieve higher resolution. SIM introduces a resolution improvement of factor 2 and quantum correlation alone a factor of \sqrt{k} , where k is the correlation order or photon-number correlation. Quantum correlation combined with SIM could lead to an improvement scaling as $k + \sqrt{k}$.¹⁶⁷ The use of photon antibunching of single emitters to obtain subdiffraction localization of pairs of quantum emitters of unknown relative intensity has been proposed. Specifically, the localization can be reconstructed by three separate Hanbury Brown and Twiss measurements.¹⁶⁸ This problem is impossible to solve based on intensity measurements alone. Two single emitters within the diffraction limit with different intensities can provide $g^2(0) < 0.5$ in a diffraction-limited image.

9 Conclusions and Outlook

In Table 2, we summarize the main results of SRM using CCs in diamond, SiC, and hBN with the achieved resolution and when spin nanoscopy has been achieved with the related magnetic

Table 2 Super-resolution and their spin variant techniques based on CCs with achieved subdiffraction resolution and magnetic imaging localization resolution and magnetic field sensitivity.

System (CC)	Method (magnetic field sensitivity) (nT/ $\sqrt{\text{Hz}}$)	Resolution (magnetic imaging) (nm)
NV C-bulk	STED	5.8 to 80 ²⁹
NV C-bulk	Spin-STED (ODMR and Rabi)	>100 ⁴⁵
NV C-bulk	SIL-STED	2.4 ¹¹²
NV NDs	STED	10 to 40 ^{32,114}
NV NDs	Spin-STED (ODMR)	>40 ¹¹⁴
NVN C-bulk	STED	50 ¹⁰⁶
NV or NVN NDs in cells	STED	50 to 70 ^{76,101}
NV C-bulk	CSD	4.1 ³⁵
NV C-bulk	Spin-CSD	>100 ⁹⁵
NV C-bulk	Spin-RESOFLT	35 to 50 ¹¹⁵
	Hahn-echo and magnetic sensing (250)	20 to 150 ¹¹⁵
NV C-bulk	GSD	8 to 16 ^{31,61}
NV NDs	GSD	36 ¹¹⁸
NV C-bulk	SMLM	27 to 29 ⁴⁷
NV C-bulk	Spin-SMLM (ODMR) (190000)	50 to 100 ⁴⁷
NV NDs	Super-resolution radial fluctuations and 2PM	43 ¹⁴²
NV NDs	SMLM	20 to 23 ^{33,48}
NV NDs	Spin-SMLM (ODMR) (85)	17 to 20 ⁴⁸
NV C-bulk	Single photon quantum correlation	290 ⁵⁵
SiV C-bulk	STED	89 ⁷²
hBN few layers flakes $V_B C_N$ ⁸³	STED	50 ⁸⁵
hBN few layers flakes	GSD	62 ¹¹⁹
hBN monolayer V_B ⁸³	SMLM	46 ¹²⁹
SiC 4H CAV	SMLM	50 ⁵⁹
SiC CAV 4H-NPs in cells	SMLM	18 ⁵⁹

imaging localization resolution and, if available, the associated sensitivity. From Table 2, the merits of the various CCs and the current gaps can be identified. Progress in using CCs in SRM techniques has been achieved mainly in bulk diamond with the best resolution and some cases with ND NV centers. The variability of resolution may be attributed mostly to the material, as photophysical properties of ND NVs can vary due to the presence of dopants, other impurities, strain, and surface defects. While the SiV and H3 centers in diamond are the only other centers that have so far been used in STED, achieving a lower resolution than NV. STED microscopy has also been applied using hBN emitters mainly to investigate the spectroscopy of the vibronic states of the emitters. Due to the higher stimulated emission cross-section of the SiV and hBN CCs (see Table 1), together with bright SiV sub-10-nm NDs, it is expected that further studies could provide better performance than NV in specific applications for biological samples with sub-50-nm features. However, the SiV in NDs may not provide the opportunity of quantum sensing as does NV. Quantum sensing using hBN flakes has not yet been demonstrated, and optical spin read-out studies in this material are in their infancy. Other CCs in diamond, such as the germanium vacancy¹⁶⁹ or nickel-related centers³⁴ available from CVD originated NDs, should be investigated for STED application, even if their properties for SRM are not yet very well-known due to the difficulty of their mass production as SP emitters and in NDs. The combination of SRM with spin control and sensing or magnetic field mapping has also progressed. Based on the above-outlined studies, it appears that deterministic methods for achieving super-resolution, such as STED, GSD, and RESOLFT, can easily enable nanoscale resolution ODMR, with GSD and RESOLFT having a better perspective due to the lower optical intensities needed. Using the GS and the MS states, issues related to loss of phase of nearby spins may be less prominent than in STED, as observed in SPIN-RESOLFT.¹¹⁵ However, it is expected that using the MS dark states in RESOLFT could also affect external spin states, thus limiting the control of nearby NVs. Two NVs at 150 nm apart were imaged. On the other hand, using a dark state as the charge state, such as NV⁰, it has been shown that the nuclear spin control is still possible.¹⁷⁰ ODMR and Rabi oscillation combined with CSD may be a better approach for spin manipulation with a subdiffraction resolution, as nuclear spin states are preserved during ionization and deionization. In CSD-ODMR, only one NV is subject to microwave control, while the other is in a different charge state, unlike in STED where all NVs are subject to microwave control. Using CSD-ODMR and Rabi oscillation, two NVs separated by 100 nm were spin manipulated.³⁵ The SMLM's method to switch off NV can also interfere less in terms of nearby external spin dephasing as in CSD. ODMR-SMLM was achieved for magnetic field imaging with subdiffraction resolution.^{47,48} Nanoscale magnetic imaging of 27 nm was achieved using spin-SMLM,⁴⁷ and the spin of two NVs was super-resolved using spin-SMLM with 23-nm resolution.⁴⁸ However, no Rabi-oscillation or spin-echo has been performed with SMLM yet. Spin-RESOLFT has enabled up to 20-nm resolution in mapping magnetic fields and 50-nm in mapping external nuclear spins. Spin-RESOLFT has achieved a sensitivity of $250 \text{ nT}/\sqrt{\text{Hz}}$ by sacrificing resolution with longer doughnut laser beam duration; while it improves resolution, it reduces the spin contrast. In spin-SMLM,⁴⁸ a higher sensitivity ($85 \text{ nT}/\sqrt{\text{Hz}}$) is achieved with longer dwell time compared with simple subdiffraction imaging localization without spin

control. In this case, sensitivity increases by increasing the number of NV centers in an ND. While improving the sensitivity to achieve nano-MRI, a dynamical decoupling sequence is applied to shallow NVs using spin-RESOLFT.¹¹⁵ Other super-resolution methods could also be explored in the future using CCs, such as the recently developed iso-STED, where adaptive optics is used to achieve sub-50-nm 3D resolution of structures in tissue.¹⁷¹ While the bulk diamond NV has provided the highest localization and resolution, its resolution in NDs is limited by the size of the NDs, and, as such, the applicability to biological samples is limited. Nevertheless, using SMLM, NV⁻ in NDs could be used for nanoscale imaging and sensing of a magnetic field in a cellular environment. Other spin quantum-controlled methods could be used in conjunction with NDs to increase the applicability of these techniques in resolving biological samples. The need for improving the quality of NDs is not only in reducing the size while maintaining the spin and optical properties required, but also to better control their nitrogen doping. Controlling the nitrogen doping in NDs is relevant for the application of NDs in MS state depletion, GSD, RESOLFT, and CSD microscopy. In particular, CSD using ND NV centers has not yet been demonstrated and could be applied with quantum sensing and a lower optical excitation power to biological samples. While FNDs are presently not suitable to super-resolve nanometric size objects due to their 25-nm sizes, other nanomaterials such as SiC NPs and hBN flakes could be better used in the super-resolution of nanometric features. However, the application of SRM in SiC NPs is still limited to only one demonstration in still large particles. In hBN, the variety of CCs of yet not fully known origin or controlled fabrication can limit its current applicability to specific biological samples investigations; however, SMLM and STED in hBN have provided an understanding of the chemical properties of the hBN defects. Both SiC and hBN have the potential to apply spin nanoscopy methods as for the NV⁻ in diamond. However, the current CCs used for SMLM and STED have not yet been studied from the point of view of spin optical read-out and control in nanomaterials, or they have a very small ODMR signature, which makes their use in spin nanoscopy currently difficult. As such, more fundamental studies on these materials' other CCs are required to determine their full potential in SRM.

Quantum optics methods based on SP emission and second and higher-order photons correlation measurements have been recently implemented, and only one demonstration was applied to the NV in bulk diamond. While these methods based on their current implementation in colloidal QDs show promise in speeding up and extending applicability as an example of SMLM to nonblinking emitters, so far their performances are limited at the best to a factor of 2 resolution improvement ($\approx 120 \text{ nm}$) compared with confocal scanning microscopy and still far from the sub-50-nm resolution of the current state-of-the-art SMLM. Nevertheless, these methods appear promising because of the fast occurring technological advances in SP detectors' time resolution and should be investigated more in the space of CCs, for example, in hBN, where the concentration of single emitters and blinking properties are favorable to quantum-enhanced-SMLM. In addition, other quantum light-based methods¹⁷² relying on quantum correlation have improved the signal-to-noise ratio in a coherent Raman microscope revealing molecular bonds within a cell, thus providing subdiffraction resolution. Such a nonlinear microscope enhanced by quantum correlation may apply to CCs in diamond or other point defects

imaging. Finally, other CCs in diamond and SiC could be investigated for super-resolution imaging combinations with quantum sensing.

References

1. L. Möckl, D. C. Lamb, and C. Bräuchle, “Super-resolved fluorescence microscopy: Nobel Prize in Chemistry 2014 for Eric Betzig, Stefan Hell, and William E. Moerner,” *Angew. Chem. Int. Ed.* **53**(51), 13972–13977 (2014).
2. L. Schermelleh et al., “Super-resolution microscopy demystified,” *Nat. Cell Biol.* **21**(1), 72–84 (2019).
3. S. Banerjee, S. Maurya, and R. Roy, “Single-molecule fluorescence imaging: generating insights into molecular interactions in virology,” *J. Biosci.* **43**(3), 519–540 (2018).
4. S. Castelletto and A. Boretti, “Viral particle imaging by super-resolution fluorescence microscopy,” *Chem. Phys. Impact* **2**, 100013 (2021).
5. S. Dhomkar et al., “Long-term data storage in diamond,” *Sci. Adv.* **2**(10), e1600911 (2016).
6. M. Gu, Q. Zhang, and S. Lamon, “Nanomaterials for optical data storage,” *Nat. Rev. Mater.* **3**(12), 16070 (2016).
7. J.-P. Tetienne et al., “Quantum imaging of current flow in graphene,” *Sci. Adv.* **3**(4), e1602429 (2017).
8. F. Casola, T. van der Sar, and A. Yacoby, “Probing condensed matter physics with magnetometry based on nitrogen-vacancy centres in diamond,” *Nat. Rev. Mater.* **3**(1), 17088 (2018).
9. D. Jin et al., “Nanoparticles for super-resolution microscopy and single-molecule tracking,” *Nat. Methods* **15**(6), 415–423 (2018).
10. I. Aharonovich et al., “Diamond-based single-photon emitters,” *Rep. Prog. Phys.* **74**(7), 076501 (2011).
11. C. Bradac et al., “Quantum nanophotonics with group IV defects in diamond,” *Nat. Commun.* **10**(1), 5625 (2019).
12. A. Gruber et al., “Scanning confocal optical microscopy and magnetic resonance on single defect centers,” *Science* **276**(5321), 2012–2014 (1997).
13. D. Ho, C.-H. K. Wang, and E. K.-H. Chow, “Nanodiamonds: the intersection of nanotechnology, drug development, and personalized medicine,” *Sci. Adv.* **3**(7), e1500439 (2015).
14. A. Lohrmann et al., “A review on single photon sources in silicon carbide,” *Rep. Prog. Phys.* **80**(3), 034502 (2017).
15. S. Castelletto and A. Boretti, “Silicon carbide color centers for quantum applications,” *J. Phys. Photonics* **2**(2), 022001 (2020).
16. S. Castelletto et al., “A silicon carbide room-temperature single-photon source,” *Nat. Mater.* **13**(2), 151–156 (2014).
17. S. Castelletto et al., “Room temperature quantum emission from cubic silicon carbide nanoparticles,” *ACS Nano* **8**(8), 7938–7947 (2014).
18. W. F. Koehl et al., “Room temperature coherent control of defect spin qubits in silicon carbide,” *Nature* **479**(7371), 84–87 (2011).
19. D. J. Christle et al., “Isolated electron spins in silicon carbide with millisecond coherence times,” *Nat. Mater.* **14**(2), 160–163 (2015).
20. A. Lohrmann et al., “Activation and control of visible single defects in 4h-, 6h-, and 3c-sic by oxidation,” *Appl. Phys. Lett.* **108**(2), 021107 (2016).
21. A. Oliveros, A. Guiseppi-Elie, and S. E. Saddow, “Silicon carbide: a versatile material for biosensor applications,” *Biomed. Microdevices* **15**(2), 353–368 (2013).
22. J. S. Ponraj et al., “SiC nanostructures toward biomedical applications and its future challenges,” *Crit. Rev. Solid State Mater. Sci.* **41**(5), 430–446 (2016).
23. T. Bělinová et al., “Immunomodulatory potential of differently-terminated ultra-small silicon carbide nanoparticles,” *Nanomaterials* **10**(3), 573 (2020).
24. F. Hayee et al., “Revealing multiple classes of stable quantum emitters in hexagonal boron nitride with correlated optical and electron microscopy,” *Nat. Mater.* **19**(5), 534–539 (2020).
25. J. D. Caldwell et al., “Photonics with hexagonal boron nitride,” *Nat. Rev. Mater.* **4**(8), 552–567 (2019).
26. C. Bradac, “High-resolution optical imaging and sensing using quantum emitters in hexagonal boron-nitride,” *Front. Phys.* **9**, 117 (2021).
27. L. Horváth et al., “*In vitro* investigation of the cellular toxicity of boron nitride nanotubes,” *ACS Nano* **5**(5), 3800–3810 (2011).
28. A. Salvetti et al., “*In vivo* biocompatibility of boron nitride nanotubes: effects on stem cell biology and tissue regeneration in planarians,” *Nanomedicine* **10**(12), 1911–1922 (2015).
29. E. Rittweger et al., “STED microscopy reveals crystal colour centres with nanometric resolution,” *Nat. Photonics* **3**(3), 144–147 (2009).
30. M. H. Alkahtani et al., “Fluorescent nanodiamonds: past, present, and future,” *Nanophotonics* **7**(8), 1423–1453 (2018).
31. E. Rittweger, D. Wildanger, and S. W. Hell, “Far-field fluorescence nanoscopy of diamond color centers by ground state depletion,” *Europhys. Lett.* **86**(1), 14001 (2009).
32. K. Y. Han et al., “Three-dimensional stimulated emission depletion microscopy of nitrogen-vacancy centers in diamond using continuous-wave light,” *Nano Lett.* **9**(9), 3323–3329 (2009).
33. M. Gu et al., “Super-resolving single nitrogen vacancy centers within single nanodiamonds using a localization microscope,” *Opt. Express* **21**(15), 17639–17646 (2013).
34. S. Castelletto et al., “Production of multiple diamond-based single-photon sources,” *IEEE J. Sel. Top. Quantum Electron.* **18**(6), 1792–1798 (2012).
35. X. Chen et al., “Subdiffraction optical manipulation of the charge state of nitrogen vacancy center in diamond,” *Light Sci. Appl.* **4**(1), e230 (2015).
36. K. Arai et al., “Fourier magnetic imaging with nanoscale resolution and compressed sensing speed-up using electronic spins in diamond,” *Nat. Nanotechnol.* **10**(10), 859–864 (2015).
37. H. Mamin et al., “Nanoscale nuclear magnetic resonance with a nitrogen-vacancy spin sensor,” *Science* **339**(6119), 557–560 (2013).
38. J. Wrachtrup and F. Jelezko, “Processing quantum information in diamond,” *J. Phys. Condens. Matter* **18**(21), S807–S824 (2006).
39. L. Childress et al., “Fault-tolerant quantum communication based on solid-state photon emitters,” *Phys. Rev. Lett.* **96**(7), 070504 (2006).
40. N. Bar-Gill et al., “Solid-state electronic spin coherence time approaching one second,” *Nat. Commun.* **4**(1), 1743 (2013).
41. D. Farfurnik et al., “Optimizing a dynamical decoupling protocol for solid-state electronic spin ensembles in diamond,” *Phys. Rev. B* **92**(6), 060301 (2015).
42. A. Boretti et al., “Nitrogen-vacancy centers in diamond for nanoscale magnetic resonance imaging applications,” *Beilstein J. Nanotechnol.* **10**(1), 2128–2151 (2019).
43. J. L. Webb et al., “Optimization of a diamond nitrogen vacancy centre magnetometer for sensing of biological signals,” *Front. Phys.* **8**, 430 (2020).
44. E. Bernardi et al., “A biocompatible technique for magnetic field sensing at (sub)cellular scale using nitrogen-vacancy centers,” *EPJ Quantum Technol.* **7**(1), 13 (2020).
45. D. Wildanger, J. R. Maze, and S. W. Hell, “Diffraction unlimited all-optical recording of electron spin resonances,” *Phys. Rev. Lett.* **107**(1), 017601 (2011).
46. P. C. Maurer et al., “Far-field optical imaging and manipulation of individual spins with nanoscale resolution,” *Nat. Phys.* **6**(11), 912–918 (2010).
47. M. Pfender et al., “Single-spin stochastic optical reconstruction microscopy,” *Proc. Natl. Acad. Sci. U. S. A.* **111**(41), 14669–14674 (2014).
48. M. Barbiero et al., “Spin-manipulated nanoscopy for single nitrogen-vacancy center localizations in nanodiamonds,” *Light Sci. Appl.* **6**(11), e17085 (2017).

49. M. Barbiero et al., "Nanoscale magnetic imaging enabled by nitrogen vacancy centres in nanodiamonds labelled by iron-oxide nanoparticles," *Nanoscale* **12**(16), 8847–8857 (2020).
50. A. Boretti and S. Castelletto, "Nanometric resolution magnetic resonance imaging methods for mapping functional activity in neuronal networks," *MethodsX* **3**, 297–306 (2016).
51. P. Wang et al., "Nanoscale magnetic imaging of ferritins in a single cell," *Sci. Adv.* **5**(4), eaau8038 (2019).
52. M. S. Grinolds et al., "Nanoscale magnetic imaging of a single electron spin under ambient conditions," *Nat. Phys.* **9**(4), 215–219 (2013).
53. M. J. Ku et al., "Imaging viscous flow of the Dirac fluid in graphene," *Nature* **583**(7817), 537–541 (2020).
54. O. Schwartz et al., "Superresolution microscopy with quantum emitters," *Nano Lett.* **13**(12), 5832–5836 (2013).
55. D. G. Monticone et al., "Beating the Abbe diffraction limit in confocal microscopy via nonclassical photon statistics," *Phys. Rev. Lett.* **113**(14), 143602 (2014).
56. M. Aßmann, "Quantum-optimally enhanced storm (QUEST) for multi-emitter localization," *Sci. Rep.* **8**(1), 7829 (2018).
57. R. Tenne et al., "Super-resolution enhancement by quantum image scanning microscopy," *Nat. Photonics* **13**(2), 116–122 (2019).
58. Y. Nishimura et al., "Wide-field fluorescent nanodiamond spin measurements toward real-time large-area intracellular thermometry," *Sci. Rep.* **11**(1), 4248 (2021).
59. S. Castelletto et al., "Imaging with nanometer resolution using optically active defects in silicon carbide," *Phys. Rev. Appl.* **14**(3), 034021 (2020).
60. S. Pezzagna et al., "Nanoscale engineering and optical addressing of single spins in diamond," *Small* **6**(19), 2117–2121 (2010).
61. K. Y. Han et al., "Metastable dark states enable ground state depletion microscopy of nitrogen vacancy centers in diamond with diffraction-unlimited resolution," *Nano Lett.* **10**(8), 3199–3203 (2010).
62. E. Herbschleb et al., "Ultra-long coherence times amongst room-temperature solid-state spins," *Nat. Commun.* **10**(1), 3766 (2019).
63. J. Stortebom et al., "Lifetime investigation of single nitrogen vacancy centres in nanodiamonds," *Opt. Express* **23**(9), 11327–11333 (2015).
64. C. Kurtsiefer et al., "Stable solid-state source of single photons," *Phys. Rev. Lett.* **85**(2), 290–293 (2000).
65. F. A. Inam et al., "Emission and nonradiative decay of nanodiamond NV centers in a low refractive index environment," *ACS Nano* **7**(5), 3833–3843 (2013).
66. A. Mohtashami and A. F. Koenderink, "Suitability of nanodiamond nitrogen-vacancy centers for spontaneous emission control experiments," *New J. Phys.* **15**(4), 043017 (2013).
67. T. Plakhotnik and H. Aman, "NV-centers in nanodiamonds: how good they are," *Diam. Relat. Mater.* **82**, 87–95 (2018).
68. P. Reineck et al., "Not all fluorescent nanodiamonds are created equal: a comparative study," *Part. Part. Syst. Char.* **36**(3), 1900009 (2019).
69. H. S. Knowles, D. M. Kara, and M. Atatüre, "Observing bulk diamond spin coherence in high-purity nanodiamonds," *Nat. Mater.* **13**(1), 21–25 (2014).
70. A. V. Turukhin et al., "Picosecond photoluminescence decay of si-doped chemical-vapor-deposited diamond films," *Phys. Rev. B* **54**(23), 16448–16451 (1996).
71. C. Wang et al., "Single photon emission from SIV centres in diamond produced by ion implantation," *J. Phys. B* **39**(1), 37–41 (2005).
72. Y. Silani, F. Hubert, and V. M. Acosta, "Stimulated emission depletion microscopy with diamond silicon vacancy centers," *ACS Photonics* **6**(10), 2577–2582 (2019).
73. L. J. Rogers et al., "All-optical initialization, readout, and coherent preparation of single silicon-vacancy spins in diamond," *Phys. Rev. Lett.* **113**(26), 263602 (2014).
74. E. Neu, M. Agio, and C. Becher, "Photophysics of single silicon vacancy centers in diamond: implications for single photon emission," *Opt. Express* **20**(18), 19956–19971 (2012).
75. E. Neu et al., "Single photon emission from silicon-vacancy colour centres in chemical vapour deposition nano-diamonds on iridium," *New J. Phys.* **13**(2), 025012 (2011).
76. G. Laporte and D. Psaltis, "STED imaging of green fluorescent nanodiamonds containing nitrogen-vacancy-nitrogen centers," *Biomed. Opt. Express* **7**(1), 34–44 (2016).
77. J.-H. Hsu et al., "Nonblinking green emission from single H3 color centers in nanodiamonds," *Appl. Phys. Lett.* **98**(19), 193116 (2011).
78. D. Beke et al., "Room-temperature defect qubits in ultrasmall nanocrystals," *J. Phys. Chem. Lett.* **11**(5), 1675–1681 (2020).
79. J.-F. Wang et al., "Experimental optical properties of single nitrogen vacancy centers in silicon carbide at room temperature," *ACS Photonics* **7**(7), 1611–1616 (2020).
80. J.-F. Wang et al., "Coherent control of nitrogen-vacancy center spins in silicon carbide at room temperature," *Phys. Rev. Lett.* **124**(22), 223601 (2020).
81. Z. Mu et al., "Coherent manipulation with resonant excitation and single emitter creation of nitrogen vacancy centers in 4H silicon carbide," *Nano Lett.* **20**(8), 6142–6147 (2020).
82. R. N. E. Malein et al., "Stimulated emission depletion spectroscopy of color centers in hexagonal boron nitride," *ACS Photonics* **8**(4), 1007–1012 (2021).
83. N. Mendelson et al., "Identifying carbon as the source of visible single-photon emission from hexagonal boron nitride," *Nat. Mater.* **20**(3), 321–328 (2021).
84. M. K. Boll et al., "Photophysics of quantum emitters in hexagonal boron-nitride nano-flakes," *Opt. Express* **28**(5), 7475–7487 (2020).
85. P. Khatri et al., "Stimulated emission depletion microscopy with color centers in hexagonal boron nitride," *ACS Photonics* **8**(7), 2081–2087 (2021).
86. A. Gottscholl et al., "Initialization and read-out of intrinsic spin defects in a van der Waals crystal at room temperature," *Nat. Mater.* **19**(5), 540–545 (2020).
87. A. Gottscholl et al., "Room temperature coherent control of spin defects in hexagonal boron nitride," *Sci. Adv.* **7**(14), eabf3630 (2021).
88. S. W. Hell and J. Wichmann, "Breaking the diffraction resolution limit by stimulated emission: stimulated-emission-depletion fluorescence microscopy," *Opt. Lett.* **19**(11), 780–782 (1994).
89. S. W. Hell and M. Kroug, "Ground-state-depletion fluorescence microscopy: a concept for breaking the diffraction resolution limit," *Appl. Phys. B* **60**(5), 495–497 (1995).
90. S. Bretschneider, C. Eggeling, and S. W. Hell, "Breaking the diffraction barrier in fluorescence microscopy by optical shelving," *Phys. Rev. Lett.* **98**(21), 218103 (2007).
91. M. Hofmann et al., "Breaking the diffraction barrier in fluorescence microscopy at low light intensities by using reversibly photoswitchable proteins," *Proc. Natl. Acad. Sci. U. S. A.* **102**(49), 17565–17569 (2005).
92. M. G. L. Gustafsson, "Surpassing the lateral resolution limit by a factor of two using structured illumination microscopy," *J. Microsc.* **198**(2), 82–87 (2000).
93. E. Betzig et al., "Imaging intracellular fluorescent proteins at nanometer resolution," *Science* **313**(5793), 1642–1645 (2006).
94. S. Hess, T. Girirajan, and M. Mason, "Ultra-high resolution imaging by fluorescence photoactivation localization microscopy," *Biophys. J.* **91**(11), 4258–4272 (2006).
95. B. Huang, M. Bates, and X. Zhuang, "Super-resolution fluorescence microscopy," *Annu. Rev. Biochem.* **78**(1), 993–1016 (2009).
96. G. Huszka and M. A. Gijs, "Super-resolution optical imaging: a comparison," *Micro Nano Eng.* **2**, 7–28 (2019).
97. G. Vicidomini, P. Bianchini, and A. Diaspro, "STED super-resolved microscopy," *Nat. Methods* **15**(3), 173–182 (2018).

98. U. V. Nägerl et al., “Live-cell imaging of dendritic spines by STED microscopy,” *Proc. Natl. Acad. Sci. U. S. A.* **105**(48), 18982–18987 (2008).
99. F. Bottanelli et al., “Two-colour live-cell nanoscale imaging of intracellular targets,” *Nat. Commun.* **7**(1), 10778 (2016).
100. N. H. Revelo and S. O. Rizzoli, “Application of sted microscopy to cell biology questions,” in *Advanced Fluorescence Microscopy*, P. Verveer, Ed., Vol. 1251, pp. 213–230, Humana Press, New York (2015).
101. Y.-K. Tzeng et al., “Superresolution imaging of albumin-conjugated fluorescent nanodiamonds in cells by stimulated emission depletion,” *Angew. Chem. Int. Ed.* **50**(10), 2262–2265 (2011).
102. N. Prabhakar et al., “Sted-tem correlative microscopy leveraging nanodiamonds as intracellular dual-contrast markers,” *Small* **14**(5), 1701807 (2018).
103. P. A. Pellett et al., “Two-color sted microscopy in living cells,” *Biomed. Opt. Express* **2**(8), 2364–2371 (2011).
104. N. Prabhakar et al., “Fluorescent and electron-dense green color emitting nanodiamonds for single-cell correlative microscopy,” *Molecules* **25**(24), 5897 (2020).
105. F.-J. Hsieh et al., “Correlative light-electron microscopy of lipid-encapsulated fluorescent nanodiamonds for nanometric localization of cell surface antigens,” *Anal. Chem.* **90**(3), 1566–1571 (2018).
106. R. Kolesov et al., “Superresolution microscopy of single rare-earth emitters in YAG and H3 centers in diamond,” *Phys. Rev. Lett.* **120**(3), 033903 (2018).
107. S. V. Bolshedvorskii et al., “Single silicon vacancy centers in 10 nm diamonds for quantum information applications,” *ACS Appl. Nano Mater.* **2**(8), 4765–4772 (2019).
108. M. D. Torelli, N. A. Nunn, and O. A. Shenderova, “A perspective on fluorescent nanodiamond bioimaging,” *Small* **15**(48), 1902151 (2019).
109. J. Jeske et al., “Stimulated emission from nitrogen-vacancy centres in diamond,” *Nat. Commun.* **8**(1), 14000 (2017).
110. A. Sajid, M. J. Ford, and J. R. Reimers, “Single-photon emitters in hexagonal boron nitride: a review of progress,” *Rep. Prog. Phys.* **83**(4), 044501 (2020).
111. S. Castelletto et al., “Hexagonal boron nitride: a review of the emerging material platform for single-photon sources and the spin-photon interface,” *Beilstein J. Nanotechnol.* **11**(1), 740–769 (2020).
112. D. Wildanger et al., “Solid immersion facilitates fluorescence microscopy with nanometer resolution and sub-Ångström emitter localization,” *Adv. Mater.* **24**(44), OP309–OP313 (2012).
113. F. Jelezko et al., “Observation of coherent oscillations in a single electron spin,” *Phys. Rev. Lett.* **92**(7), 076401 (2004).
114. S. Arroyo-Camejo et al., “Stimulated emission depletion microscopy resolves individual nitrogen vacancy centers in diamond nanocrystals,” *ACS Nano* **7**(12), 10912–10919 (2013).
115. J.-C. Jaskula et al., “Superresolution optical magnetic imaging and spectroscopy using individual electronic spins in diamond,” *Opt. Express* **25**(10), 11048–11064 (2017).
116. H. Zhang et al., “Selective addressing of solid-state spins at the nanoscale via magnetic resonance frequency encoding,” *npj Quantum Inf.* **3**(1), 31 (2017).
117. I. Testa et al., “Nanoscopy of living brain slices with low light levels,” *Neuron* **75**(6), 992–1000 (2012).
118. J. Stortorboom et al., “Ground-state depletion nanoscopy of nitrogen-vacancy centres in nanodiamonds,” *Nanoscale Res. Lett.* **16**, 44 (2021).
119. M. Kianinia et al., “All-optical control and super-resolution imaging of quantum emitters in layered materials,” *Nat. Commun.* **9**(1), 874 (2018).
120. X. Yang et al., “Sub-diffraction imaging of nitrogen-vacancy centers in diamond by stimulated emission depletion and structured illumination,” *RSC Adv.* **4**(22), 11305–11310 (2014).
121. S. A. Jones et al., “Fast, three-dimensional super-resolution imaging of live cells,” *Nat. Methods* **8**(6), 499–505 (2011).
122. R. Strack, “Deep learning advances super-resolution imaging,” *Nat. Methods* **15**(6), 403 (2018).
123. F. Wang et al., “Editorial: recent advances in fluorescent probes for super-resolution microscopy,” *Front. Chem.* **9**, 698531 (2021).
124. E. Nehme et al., “Deep-storm: super-resolution single-molecule microscopy by deep learning,” *Optica* **5**(4), 458–464 (2018).
125. M. Alkahtani et al., “Growth of high-purity low-strain fluorescent nanodiamonds,” *ACS Photonics* **6**(5), 1266–1271 (2019).
126. M. Motlag et al., “Molecular-scale nanodiamond with high-density color centers fabricated from graphite by laser shocking,” *Cell Rep. Phys. Sci.* **3**(5), 100054 (2020).
127. C. Laube et al., “Controlling the fluorescence properties of nitrogen vacancy centers in nanodiamonds,” *Nanoscale* **11**(4), 1770–1783 (2019).
128. Y. Huang et al., “Superresolution localization of nitrogen-vacancy centers in diamond with quantum-controlled photo-switching,” *Phys. Rev. A* **102**(4), 040601 (2020).
129. J. Feng et al., “Imaging of optically active defects with nanometer resolution,” *Nano Lett.* **18**(3), 1739–1744 (2018).
130. J. Comtet et al., “Wide-field spectral super-resolution mapping of optically active defects in hexagonal boron nitride,” *Nano Lett.* **19**(4), 2516–2523 (2019).
131. N. M. H. Duong et al., “Facile production of hexagonal boron nitride nanoparticles by cryogenic exfoliation,” *Nano Lett.* **19**(8), 5417–5422 (2019).
132. J. Comtet et al., “Direct observation of water-mediated single-proton transport between HBN surface defects,” *Nat. Nanotechnol.* **15**(7), 598–604 (2020).
133. F. Chen et al., “Cellular toxicity of silicon carbide nanomaterials as a function of morphology,” *Biomaterials* **179**, 60–70 (2018).
134. F. Helmchen and W. Denk, “Deep tissue two-photon microscopy,” *Nat. Methods* **2**(12), 932–940 (2005).
135. T. J. Gould et al., “Adaptive optics enables 3D STED microscopy in aberrating specimens,” *Opt. Express* **20**(19), 20998–21009 (2012).
136. T.-L. Wee et al., “Two-photon excited fluorescence of nitrogen-vacancy centers in proton-irradiated type Ib diamond,” *J. Phys. Chem. A* **111**(38), 9379–9386 (2007).
137. P. Ji et al., “Multiple-photon excitation of nitrogen vacancy centers in diamond,” *Phys. Rev. B* **97**(13), 134112 (2018).
138. Y.-R. Chang et al., “Mass production and dynamic imaging of fluorescent nanodiamonds,” *Nat. Nanotechnol.* **3**(5), 284–288 (2008).
139. C. M. Jimenez et al., “Nanodiamond-PMO for two-photon PDT and drug delivery,” *J. Mater. Chem. B* **4**(35), 5803–5808 (2016).
140. Y. Y. Hui et al., “Two-photon fluorescence correlation spectroscopy of lipid-encapsulated fluorescent nanodiamonds in living cells,” *Opt. Express* **18**, 5896–5905 (2010).
141. M. Barbiero, S. Castelletto, and M. Gu, “Multi-focal laser fabrication of nitrogen vacancy centers in a bulk diamond,” *OSA Continuum* **3**(12), 3416–3423 (2020).
142. G. E. Johnstone, G. S. Cairns, and B. R. Patton, “Nanodiamonds enable adaptive-optics enhanced, super-resolution, two-photon excitation microscopy,” *R. Soc. Open Sci.* **6**(7), 190589 (2019).
143. S. Culley et al., “SRRF: universal live-cell super-resolution microscopy,” *Int. J. Biochem. Cell Biol.* **101**, 74–79 (2018).
144. N. Gustafsson et al., “Fast live-cell conventional fluorophore nanoscopy with imagej through super-resolution radial fluctuations,” *Nat. Commun.* **7**(1), 12471 (2016).
145. A. W. Schell et al., “Non-linear excitation of quantum emitters in hexagonal boron nitride multiplayers,” *APL Photonics* **3**(9), 091302 (2016).
146. M. Alkahtani and P. Hemmer, “Charge stability of nitrogen-vacancy color centers in organic nanodiamonds,” *Opt. Mater. Express* **10**(5), 1224–1231 (2020).

147. N. Aslam et al., "Photo-induced ionization dynamics of the nitrogen vacancy defect in diamond investigated by single-shot charge state detection," *New J. Phys.* **15**(1), 013064 (2013).
148. P. Siyushev et al., "Optically controlled switching of the charge state of a single nitrogen-vacancy center in diamond at cryogenic temperatures," *Phys. Rev. Lett.* **110**(16), 167402 (2013).
149. Y. Doi et al., "Pure negatively charged state of the NV center in n-type diamond," *Phys. Rev. B* **93**(8), 081203 (2016).
150. E. Bauch et al., "Ultralong dephasing times in solid-state spin ensembles via quantum control," *Phys. Rev. X* **8**(3), 031025 (2018).
151. S. Li et al., "Optical far-field super-resolution microscopy using nitrogen vacancy center ensemble in bulk diamond," *Appl. Phys. Lett.* **109**(11), 111107 (2016).
152. X.-D. Chen et al., "Near-infrared-enhanced charge-state conversion for low-power optical nanoscopy with nitrogen-vacancy centers in diamond," *Phys. Rev. Appl.* **7**(1), 014008 (2017).
153. D.-F. Li et al., "Low power charge state depletion nanoscopy of the defect in diamonds with a pulsed laser excitation," *Opt. Lett.* **45**(3), 730–733 (2020).
154. X.-D. Chen et al., "Superresolution multifunctional sensing with the nitrogen-vacancy center in diamond," *Phys. Rev. Appl.* **12**(4), 044039 (2019).
155. T. Gregory et al., "Imaging through noise with quantum illumination," *Sci. Adv.* **6**(6), eaay2652 (2020).
156. P.-A. Moreau et al., "Imaging with quantum states of light," *Nat. Rev. Phys.* **3**(6), 367–380 (2019).
157. S. W. Hell, J. Soukka, and P. E. Hänninen, "Two- and multiphoton detection as an imaging mode and means of increasing the resolution in far-field light microscopy: a study based on photon-optics," *Bioimaging* **3**(2), 64–69 (1995).
158. P. Hong and G. Zhang, "A review of super-resolution imaging through optical high-order interference [invited]," *Appl. Sci.* **9**(6), 1166 (2019).
159. H. J. Kimble, M. Dagenais, and L. Mandel, "Photon antibunching in resonance fluorescence," *Phys. Rev. Lett.* **39**(11), 691–695 (1977).
160. O. Schwartz and D. Oron, "Improved resolution in fluorescence microscopy using quantum correlations," *Phys. Rev. A* **85**(3), 033812 (2012).
161. T. Dertinger et al., "Fast, background-free, 3D super-resolution optical fluctuation imaging (SOFI)," *Proc. Natl. Acad. Sci.* **106**(52), 22287–22292 (2009).
162. G. Lubin et al., "Quantum correlation measurement with single photon avalanche diode arrays," *Opt. Express* **27**(23), 32863–32882 (2019).
163. Y. Israel et al., "Quantum correlation enhanced super-resolution localization microscopy enabled by a fibre bundle camera," *Nat. Commun.* **8**(1), 14786 (2017).
164. U. Rossman et al., "Rapid quantum image scanning microscopy by joint sparse reconstruction," *Optica* **6**(10), 1290–1296 (2019).
165. C. B. Müller and J. Enderlein, "Image scanning microscopy," *Phys. Rev. Lett.* **104**(19), 198101 (2010).
166. C. J. Sheppard, S. B. Mehta, and R. Heintzmann, "Super-resolution by image scanning microscopy using pixel reassignment," *Opt. Lett.* **38**(15), 2889–2892 (2013).
167. A. Classen et al., "Superresolution via structured illumination quantum correlation microscopy," *Optica* **4**(6), 580–587 (2017).
168. J. G. Worboys, D. W. Drumm, and A. D. Greentree, "Quantum multilateration: subdiffraction emitter pair localization via three spatially separate Hanbury Brown and Twiss measurements," *Phys. Rev. A* **101**(1), 013810 (2020).
169. T. Iwasaki et al., "Germanium-vacancy single color centers in diamond," *Sci. Rep.* **5**(1), 12882 (2015).
170. G. Waldherr et al., "Dark states of single nitrogen-vacancy centers in diamond unraveled by single shot NMR," *Phys. Rev. Lett.* **106**(15), 157601 (2011).
171. X. Hao et al., "Three-dimensional adaptive optical nanoscopy for thick specimen imaging at sub-50-nm resolution," *Nat. Methods* **18**(6), 688–693 (2021).
172. C. A. Casacio et al., "Quantum-enhanced nonlinear microscopy," *Nature* **594**(7862), 201–206 (2021).

Stefania Castelletto is a professor of engineering at RMIT University. She received her degree in physics from the University of Turin in 1992 and her PhD in quantum metrology from the Polytechnic of Turin University in 1998. She is the author of more than 160 journal articles and three book chapters. Her current research interests include super-resolution in nanodiamonds and silicon carbide, color centers in diamond, and silicon carbide for quantum technologies.

Alberto Boretti completed his PhD in energy engineering in 1988. He has been a senior researcher and manager in the automotive industry in Italy for 17 years. Then, he has been a senior research fellow, and engineering associate professor, professor, and head of a department, in universities in Australia, USA, and GCC countries for 15 years. He is currently dean of research and graduates' studies. He has published so far about 370 articles in refereed journals, mostly single-author, plus book, book chapters, patents, and conference papers, in various fields of science and engineering.